In this case $\mathbf{k}\mathbf{R}_s+\mathbf{l}\mathbf{R}_r=\mathbf{k}+\mathbf{l}$ so that (A.4) may be simplified to

$$\langle E_{\mathbf{h}}E_{\mathbf{k}}E_{\mathbf{l}}\rangle=\frac{1}{(N_{\mathrm{eq}})_{\mathrm{pr}}^{1/2}}\,\frac{1}{(\varepsilon_{\mathbf{h}}\varepsilon_{\mathbf{k}}\varepsilon_{\mathbf{l}})^{1/2}}\sum{}'' \exp\,[i\Delta_{s,r}]. \qquad (A.5)$$

According to (5) the expected value of $\Phi=\varphi_{\mathbf{h}}+\varphi_{\mathbf{k}}+\varphi_{\mathbf{l}}$ is then defined by

$$\tan\,\Delta_f=(\textstyle\sum''\sin\,\Delta_{s,r})/(\sum''\cos\,\Delta_{s,r})=T/B$$

where $\Delta_{s,r}=+2\pi(\mathbf{k}\mathbf{T}_s+\mathbf{l}\mathbf{T}_r)$. Accordingly, the reliability parameter of the phase estimate is given by

$$G'=\frac{2|E_{\mathbf{h}}E_{\mathbf{k}}E_{\mathbf{l}}|}{(N_{\mathrm{eq}})_{\mathrm{pr}}^{1/2}}\,\frac{1}{(\varepsilon_{\mathbf{h}}\varepsilon_{\mathbf{k}}\varepsilon_{\mathbf{l}})^{1/2}}\,(T^2+B^2)^{1/2} \qquad (A.6)$$

Finally, the conditional probability distribution of Φ given $|E_{\mathbf{h}}|, |E_{\mathbf{k}}|, |E_{\mathbf{l}}|$ in any space group and for any triple $(\mathbf{h},\mathbf{k},\mathbf{l})$ is given by

$$P(\Phi\,||E_{\mathbf{h}}E_{\mathbf{k}}E_{\mathbf{l}}|)$$
$$=[2\pi I_0(G')]\exp\,[G'\cos\,(\Phi-\Delta_f)]. \qquad (A.7)$$

Even if explicitly obtained for non-centric phase triplets, these results are easily extended to any kind of triplet with three-phase restricted structure factors. Indeed, the expected value of Φ will always be defined by $\tan\,\Delta f$: a hyperbolic tangent expression can then define which of the two allowed phase values is more probable (see § 2).

References

Burla, M. C., Camalli, M., Cascarano, G., Giacovazzo, C., Polidori, G., Spagna, R. & Viterbo, D. (1989). *J. Appl. Cryst.* **22**, 389-393.

Castleden, I. R. (1987). *Acta Cryst.* **A43**, 384-393.

Cochran, W. (1955). *Acta Cryst.* **8**, 473-478.

Giacovazzo, C. (1974*a*). *Acta Cryst.* **A30**, 626-630.

Giacovazzo, C. (1974*b*). *Acta Cryst.* **A30**, 631-634.

Giacovazzo, C. (1976). *Acta Cryst.* **A32**, 958-966.

Giacovazzo, C. (1989). *Acta Cryst.* **A45**, 534-538.

Giacovazzo, C. & Vicković, I. (1980). *Acta Cryst.* **A36**, 1017-1025.

Han, F. & Langs, D. A. (1988). *Acta Cryst.* **A44**, 563-566.

Hauptman, H. & Green, E. A. (1978). *Acta Cryst.* **A34**, 224-229.

Hauptman, H. & Karle, J. (1956). *Acta Cryst.* **9**, 635-651.

Main, P. (1985). In *Crystallographic Computing* 3: *Data Collection, Structure Determination, Proteins and Databases*, edited by G. M. Sheldrick, C. Krüger & R. Goddard, pp. 206-215. Oxford: Clarendon Press.

Peschar, R. & Schenk, H. (1987). *Acta Cryst.* **A43**, 513-522.

Pontenagel, W. M. G. F. & Krabbendam, H. (1983). *Acta Cryst.* **A39**, 333-340.

Acta Cryst. (1991). A47, 352-373

Angular Distribution of Reflections in Laue Diffraction

By D. W. J. Cruickshank

Chemistry Department, UMIST, Manchester M60 1QD, England

J. R. Helliwell

Chemistry Department, University of Manchester, Manchester M13 9PL, England, and SERC Daresbury Laboratory, Daresbury, Warrington WA4 4AD, England

and K. Moffat†

Section of Biochemistry, Molecular and Cell Biology, Biotechnology Building, Cornell University, Ithaca, New York 14853, USA

(*Received* 15 *May* 1990; *accepted* 10 *January* 1991)

Abstract

An analysis is presented of the angular distribution of reflections in Laue diffraction, with particular application to the spatial overlap problem in synchrotron macromolecular crystallography. Spatial overlaps of spots on the detector occur when the angular separations of adjacent diffracted beams are very small. The maximum density of spots occurs at $\theta_c=\sin^{-1}(\lambda_{\min}D^*/2)$ and the majority of spots in this region of θ have short wavelengths. At higher θ the mean wavelength increases steadily. On a flat detector the spots of a Laue pattern lie on intersecting conics. Each conic corresponds to a zone plane of reciprocal-

---

† Present address: Department of Biochemistry and Molecular Biology, University of Chicago, 920 E 58th Street, Chicago, IL 60637, USA.

0108-7673/91/040352-22$03.00

lattice points (RLPs), whose zone axis is represented by a point uvw in the direct lattice. If $P[uvw]$ is the distance of uvw from the origin and ψ is the angle between the zone axis and the incident beam, then the average spacing between spots on a conic is proportional to $P\sin\psi$ and the width of the clear gap bordering a conic is proportional to $1/P$. This explains why the densest conic arcs are flanked by the larger clear spaces and shows that local spatial overlap problems are inherently one dimensional in character. The vast majority of small angular separations are associated with pairs of adjacent single-order reflections. Multiples have larger separations from their nearest neighbours, which are always singles. The detailed analysis shows the factors that govern the spatial overlap of spots and indicates tactics for experimental design. The analysis is also relevant to polychromatic neutron diffraction.

1. Introduction

1.1. *Background*

The availability of synchrotron X-ray sources has renewed interest in the Laue diffraction method. The method makes optimum use of the polychromatic radiation spectrum and permits very brief exposures, even for weakly scattering crystals.

We earlier considered the multiplicity distribution of reflections in Laue diffraction (Cruickshank, Helliwell & Moffat, 1987, hereafter CHM1). When a crystal is illuminated by a polychromatic beam of X-rays, many orders of each Bragg reflection may be stimulated simultaneously and overlap exactly in scattering angle. It might be thought (Wyckoff, 1924, p. 142; Bragg, 1975, p. 137; Amorós, Buerger & Amorós, 1975, p. 13) that, with a wide wavelength range, few Laue reflections would be single: most would be multiple, arising from several orders. We showed that this fear was unjustified and that in typical situations the proportion of reciprocal-lattice points that lie on single rays always exceeds 83%.

There is another complexity of the Laue method which is of a geometrical nature. This is the so-called spatial overlap problem (Helliwell, 1985): the angular separation between diffracted beams can be so small that, because of their finite size, they lead to overlapped spots on the detector. In an initial example of a protein Laue diffraction pattern considered by Helliwell (1985), the number of spatial overlaps was comparable with the number of multiple-order energy overlaps. It is evident from simulations that as the unit-cell size is increased, for example to that typical for a virus crystal, the number of spatial overlaps considerably exceeds the number of energy overlaps. At the other extreme, for example small-molecule crystals, the number of spatial overlaps is negligible.

The spatial overlap problem is, therefore, not as general an obstacle as the energy overlap problem once appeared to be. In monochromatic methods, spatially overlapped spots are carefully prevented from occurring, either by restricting the oscillation angle in the rotation method or by simultaneously translating the film as in the Weissenberg method. Clearly if the Laue method is to be applied to very large unit cells for quantitative structure analysis, efforts have to be made to diminish the spatial overlap problem.

There are three obvious possibilities: move the detector further back; introduce computational spatial deconvolution procedures; restrict the wavelength range. Whether considering these or more novel detection schemes, it is important to understand clearly the geometric properties of Laue patterns.

We began the present work from a need to understand the spatial overlap problem. However, this paper covers a wider field and is a general analysis of the angular distribution of spots in Laue patterns and the way in which the angular distribution depends on various experimental parameters. The analysis presented builds on CHM1 explicitly. Hence, in the next subsection we recapitulate some points from CHM1. In § 2 we describe the general appearance of Laue patterns from crystals with larger unit cells. A treatment is given in § 3 of the two-dimensional density of spots on the detector; this is based on the mapping of the accessible volume of reciprocal space on to the detector. The discussion is then extended to consider the wavelength distribution on any small area of the detector.

In terms of spatial resolution, the coarse two-dimensional density does not identify the most serious aspect of the problem of the angular proximity of spots. Along the arcs approaching multiple reflections (nodals), the spots can approach each other very closely. That is, the problem is inherently one dimensional in nature. Around the nodals themselves, there are relatively large clear gaps. A qualitative description of the clear gaps in Laue patterns and of the arrangement of spots along arcs has been given by Jeffrey (1958). We analyse the effects quantitatively. This analysis is considerably more involved and far reaching than that for the coarse two-dimensional distribution and so extends from § 4 through to § 8. For example, we derive expressions for the minimum possible as well as the average separation between beams in a given zone (§ 7). We note here that there is an optimum crystal-to-plate distance: improved spatial resolution offered by increasing the distance is eventually counter-productive because of the loss of reflections that then pass outside the plate. Finally, we consider the practical implications with novel experimental schemes in § 8.

1.2. *Recapitulation*

We summarize some points and nomenclature from CHM1. For a stationary crystal and white radiation, the accessible region of reciprocal space is considered to lie between the Ewald spheres of radii $1/\lambda_{\max}$ and $1/\lambda_{\min}$. There is also a sample resolution limit $D^* = d^*_{\max} = 1/d_{\min}$ represented by a sphere of radius D^* centred at the origin. The accessible region of reciprocal space, which is cylindrically symmetrical about the incident X-ray beam, may be further limited by experimental restrictions, such as plate size, thus causing a θ cut with maximum acceptance angle $\theta_{\rm acc}$.

A *ray* is a central line in reciprocal space from $(0, 0, 0)$ passing through the RLPs $\mathbf{h} = (h, k, l)$, $2\mathbf{h}, 3\mathbf{h}, \ldots, n\mathbf{h}, \ldots$. Provided the lattice is primitive and the greatest common divisor of h, k, l is 1, then $\mathbf{h}$ is the *inner point* of the ray. $n\mathbf{h}$ is the *nth-order point* or nth harmonic. A ray of *multiplicity m* is one containing m points inside or on the surfaces of the accessible region.

CHM1 showed the probability that a RLP, randomly chosen in three dimensions, is an inner point is

$$Q = (1 - 1/2^3)(1 - 1/3^3)(1 - 1/5^3)\ldots \simeq 0{\cdot}832. \quad (1.1)$$

If the stimulated region has volume V_R and V^* is the volume of the reciprocal unit cell, then for $V_R \gg V^*$ the number of RLPs in V_R is approximately $N = V_R/V^*$ and the number of inner points in V_R is approximately $QN = QV_R/V^*$.

The volume of the accessible region defined by D^*, $\lambda_{\max}$ and $\lambda_{\min}$ is

$$V_R = (\pi/4)D^{*4}(\lambda_{\max} - \lambda_{\min}). \quad (1.2)$$

We distinguish between Laue reflections and Bragg reflections. A Bragg reflection arises from a particular order. A Laue reflection, corresponding to a spot on the detector, may arise from the superposition of several Bragg reflections generated by the accessible RLPs along a single ray.

2. General features of Laue patterns

Fig. 1(a) shows a computer simulation of a flat-plate Laue pattern for the protein pea lectin (PL 30° orientation). The spots are arranged in families of intersecting conic arcs (ellipses or hyperbolae). Some conics stand out to the eye because they have a high density of spots and are bordered by clear strips. These conics relate to zone axes of low indices. Two or more such conics intersect at spots which stand out in the centre of small clear areas. These spots are *nodals*, that is, spots of low inner indices and often of high multiplicity. Thus, in Fig. 1(a), spot a is the $1\bar{2}1$ nodal, actually of multiplicity five, corresponding to the Bragg reflections $5,\overline{10},5$; $6,\overline{12},6$; $7,\overline{14},7$; $8,\overline{16},8$; $9,\overline{18},9$. Spot b is the $0\bar{1}1$ nodal, c is $01\bar{2}$, d is $11\bar{2}$, e is $\bar{1}1\bar{2}$, f is $20\bar{1}$, g is $\bar{2}0\bar{1}$ and h is $\bar{2}\bar{1}0$. The hyperbola through f, 0 and g corresponds to the zone [010], so that the spots on it are of type $h0l$. Because of the crystal setting, the hyperbola for the [100] zone is a straight line passing through b, 0 and c and the spots on it are of type $0kl$. The small ellipse through 0 and b with very closely spaced spots corresponds to the zone [011], and the spots on it are of type $hk\bar{k}$.

If the crystal is oriented with a principal plane of the reciprocal lattice, say $k = 0$, perpendicular to the incident beam, then the Laue pattern has a clear area around the centre because the principal plane is tangential at the origin to every Ewald sphere (Henry, Lipson & Wooster, 1951). The spots with lowest θ then correspond to the intersections of the plane $k = 1$ (or -1) with the Ewald spheres. In a pattern such as Fig. 2 where the incident beam is along $\mathbf{b}$ [pea lectin (PL) 90° orientation], the central area is clear because the $k = 0$ plane is tangential to the Ewald spheres. The first group of spots outside the circular clear region is due to $k = 1$; the next apparent circle in the distribution marks the arrival of the $k = 2$ spots and the next the arrival of the $k = 3$ spots. These circular density effects are particularly obvious in Fig. 2 because there is a big difference between the orthorhombic reciprocal axes $a^* = 0{\cdot}01971$ and $c^* = 0{\cdot}00732$ Å^{-1}. This difference is also the reason why only conics for $[hk0]$ zones are visually apparent and not those for $[0kl]$ zones.

For given reciprocal-cell dimensions, the number of spatial overlaps in a pattern obviously depends on the crystal-to-plate distance and the spot centre-to-centre acceptance limit. The effect of reducing the crystal-to-plate distance from the 95 mm of Fig. 1(a) to 64 and 34 mm is shown in Figs. 1(b) and (c). The overcrowding increases dramatically. If the patterns are viewed from a distance so that details of individual conics are lost, it appears, and will be confirmed theoretically in § 3, that the number density of spots per unit area of plate increases fairly rapidly from the centre to a maximum at a certain θ and then decreases slowly towards the edge of the plate.

It is also apparent that the number density of spots per unit arc length is very high in some of the conics, even at the 95 mm crystal-to-plate distance. The [011] ellipse in Fig. 1(a) has already been pointed out.

3. Statistics of the radial distribution of reflections

3.1. *RLP distribution*

We now consider the coarse two-dimensional features of the statistical distribution of reflections in a Laue pattern and we start by examining the number of RLPs mapped per unit area of detector. Evidently this depends on the volume of reciprocal space mapped onto the detector.

In Fig. 3 let a central line from the reciprocal origin O intercept the internal surface S_i of the accessible region at I and the external surface S_e ($\lambda_{\min}$ or D^* spheres) at E. The angle between this central line and the tangent plane at O is θ. If θ_c defines the intersection of the $\lambda_{\min}$ and D^* spheres and θ_m defines the intersection of the $\lambda_{\max}$ and D^* spheres,

$$\theta_c = \sin^{-1}(\lambda_{\min}D^*/2), \qquad \theta_m = \sin^{-1}(\lambda_{\max}D^*/2).$$

From Fig. 3 we see immediately that IE lengthens as θ increases from 0 to θ_c and then decreases as θ increases towards θ_m. We shall thus not be surprised if the algebraic analysis shows that the area density of RLPs on the detector reaches a maximum when $\theta = \theta_c$.

If φ is the azimuthal angle about the incident-beam direction, a volume element of reciprocal space is given by

$$dd^*d^*\,\mathrm{d}\theta\, d^*\cos\theta\,\mathrm{d}\varphi,$$

where d^* is the distance from the origin. By integration in d^*, the accessible volume of reciprocal space bounded between θ, $\theta+\mathrm{d}\theta$ and φ, $\varphi+\mathrm{d}\varphi$ is

$$\begin{aligned}\rho^*(\theta,\varphi)\,\mathrm{d}\theta\,\mathrm{d}\varphi &= \textstyle\int d^{*2}dd^*\cos\theta\,\mathrm{d}\theta\,\mathrm{d}\varphi\\ &= (1/3)(d_e^{*3}-d_i^{*3})\cos\theta\,\mathrm{d}\theta\,\mathrm{d}\varphi.\end{aligned} \tag{3.1}$$

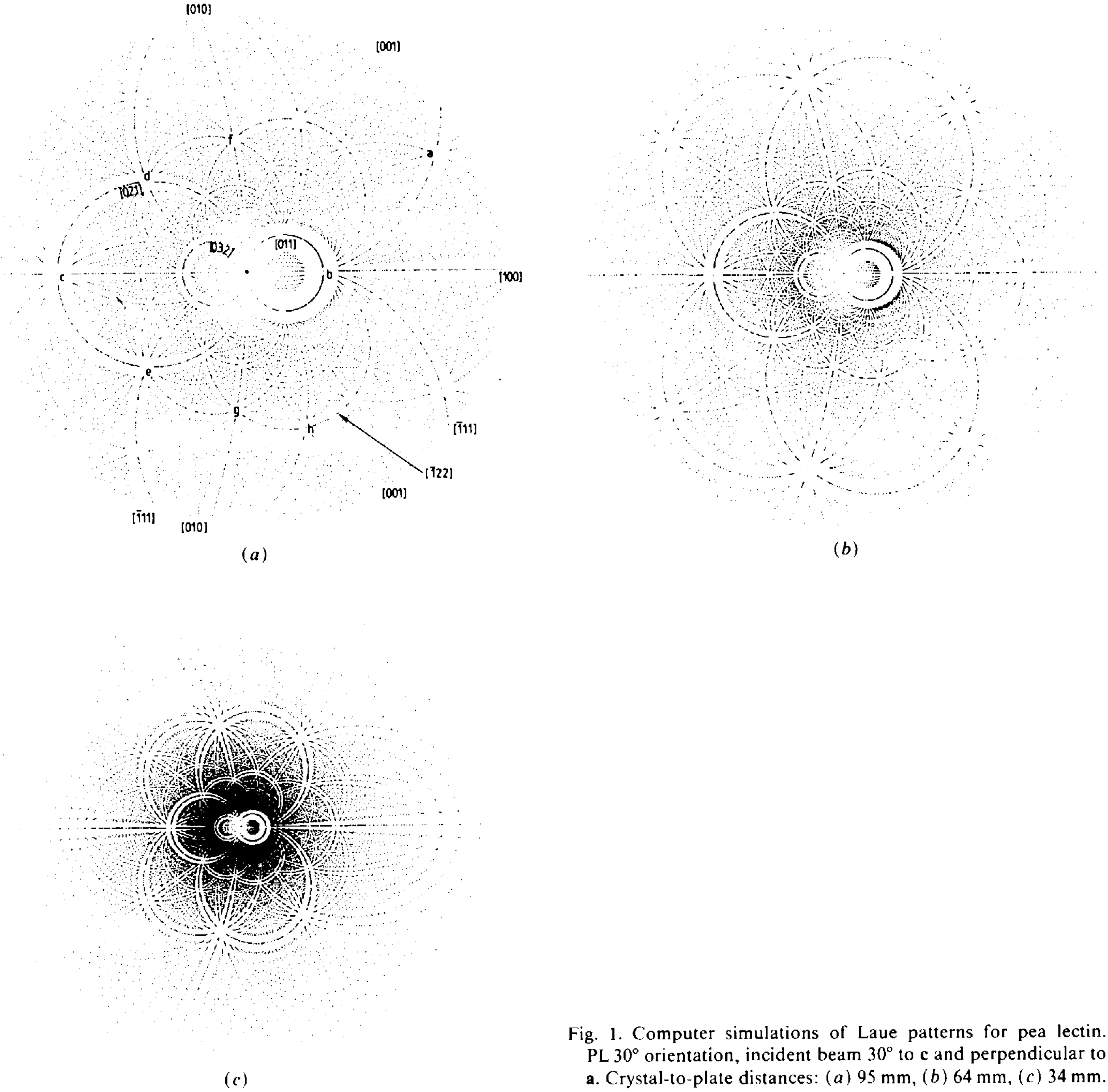

(a)

(b)

(c)

Fig. 1. Computer simulations of Laue patterns for pea lectin. PL 30° orientation, incident beam 30° to **c** and perpendicular to **a**. Crystal-to-plate distances: (a) 95 mm, (b) 64 mm, (c) 34 mm.

This volume of reciprocal space is mapped onto the detector at scattering angles between 2θ and $2\theta+\mathrm{d}(2\theta)$ and in the same azimuthal range φ, $\varphi+\mathrm{d}\varphi$. Consider a planar detector normal to the incident beam with crystal-to-plate distance CF. The area of the small piece of the circular annulus on the detector between 2θ and $2\theta+\mathrm{d}(2\theta)$ and φ to $\varphi+\mathrm{d}\varphi$ is

$$[(CF/\cos^2 2\theta)\mathrm{d}(2\theta)][CF\tan 2\theta\, \mathrm{d}\varphi],$$

since the detector element is at distances $CF/\cos 2\theta$ from the crystal and $CF\tan 2\theta$ from the incident-beam axis and the element is inclined to the diffraction direction.

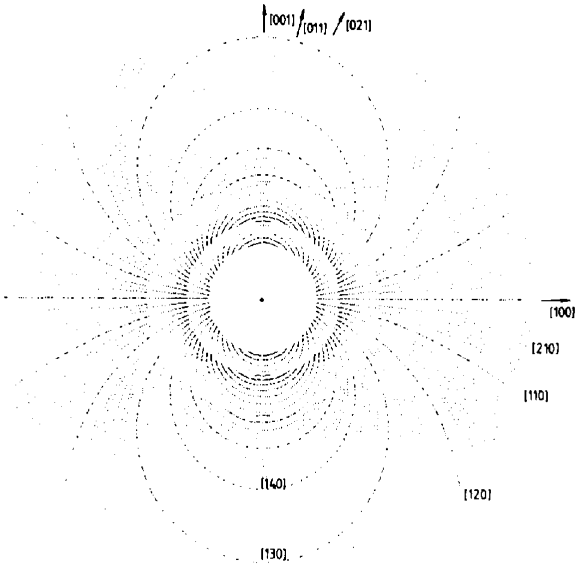

Fig. 2. Computer simulation of Laue pattern for pea lectin. PL 90° orientation, incident beam along **b**. Crystal-to-plate distance: 95 mm.

If we divide $\rho^*(\theta, \varphi)\,\mathrm{d}\theta\,\mathrm{d}\varphi$ by this area, we obtain the volume of reciprocal space mapped per unit area of the detector. If we divide further by V^*, effectively assuming an averaged orientation of the crystal, we obtain the number of RLPs mapped per unit area of the detector as

$$\frac{1}{CF^2}\frac{1}{12V^*}[d_e^{*3}-d_i^{*3}]\frac{\cos^3 2\theta}{\sin\theta}. \qquad (3.2)$$

For $\theta<\theta_c$, $d_e^*=2\sin\theta/\lambda_{\min}$ and $d_i^*=2\sin\theta/\lambda_{\max}$, so that the RLP number density varies as $\sin^2\theta\cos^3 2\theta$. For small θ the density varies as θ^2 and as θ increases the density reaches a maximum with a cusp at $\theta=\theta_c$ [unless, exceptionally, $\theta_c>\sin^{-1}(1/2\times 2^{1/2})=20{\cdot}7°$, in which case the factor $\sin^2\theta\cos^3 2\theta$ reaches a maximum for $\theta<\theta_c$]. For $\theta>\theta_c$, $d_e^*=D^*$ but d_i^* continues to increase. In consequence the density falls steadily to zero as θ increases from θ_c towards θ_m. Fig. 4 shows an example of the density as a function of θ. (If $\theta_m>45°$ back reflections are possible and the number density on an infinite normal plate will be zero for $2\theta=90°$.)

3.2. *Laue reflection distribution*

The number density for the mapping of rays, that is the number of Laue reflections or spots per unit area, will be lower than for RLPs because some reflections will be multiple. Calculations for the number of rays can be handled by the methods of CHM1. As earlier, the accessible region is considered to be bounded by an external surface S_e and an internal surface S_i. As in Fig. 3, any ray cuts S_i at distance d_i^* and S_e at distance d_e^*. Suppose the inner point **h** of this ray has reciprocal radius d_h^*. If $d_i^*\geq d_h^*\geq d_e^*$,

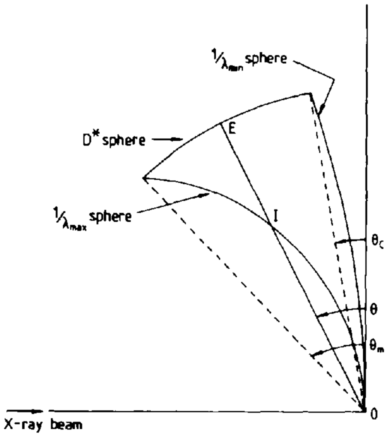

Fig. 3. Accessible region of reciprocal space. Only the upper section of the volume of revolution is shown. The internal surface S_i involves the $1/\lambda_{\max}$ sphere. The external surface S_e involves the D^* and $1/\lambda_{\min}$ spheres. The central line OIE has $OI=d_i^*$ and $OE=d_e^*$.

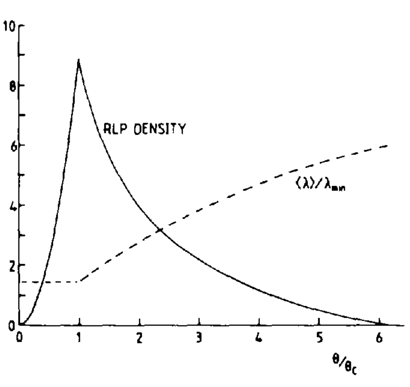

Fig. 4. Detector RLP area density (continuous curve) and mean wavelength $\langle\lambda\rangle/\lambda_{\min}$ (- - -) as functions of θ. The parameters used are $\lambda_{\max}/\lambda_{\min}=6$ and $\lambda_{\min}D^*=0{\cdot}12$, so that $\theta_c=\sin^{-1}(0{\cdot}12/2)=3{\cdot}44°$ and $\theta_m=\sin^{-1}(0{\cdot}72/2)=21{\cdot}10°=6{\cdot}13\theta_c$. The RLP density function plotted is proportional to $\sin^2\theta\cos^3 2\theta(A^3-1/216)$, where $A=1$ for $\theta<\theta_c$ and $A=0{\cdot}06/\sin\theta$ for $\theta>\theta_c$.

the ray will be accessible and will give rise to a Laue reflection.

If $d^*_h < d^*_i$, the higher orders of **h** will have reciprocal radii $2d^*_h$, $3d^*_h, \ldots$ and one or more of these orders may lie in the accessible region and so give rise to a Laue reflection. If also $d^*_e \geq 2d^*_i$, we can be certain that at least one order lies in the accessible region, for the spacing between orders is d^*_h which is less than the width $d^*_e - d^*_i$ of the accessible region.

Thus for regions in which the relation between the surfaces S_e and S_i satisfies $d^*_e \geq 2d^*_i$ on every ray, the number of accessible rays can be calculated from the shape of the external surface alone. This number is simply the number of inner points within S_e, *viz* QV^*_e/V^*, where V^*_e is the volume defined by the origin and the appropriate region of the external surface.

Consequently, by comparison with (3.2) the number of Laue reflections per unit area of a planar detector is

$$\frac{1}{CF^2}\,\frac{Q}{12V^*}\,d_e^{*3}\,\frac{\cos^3 2\theta}{\sin\theta}. \qquad (3.3)$$

This expression is valid where $d^*_e \geq 2d^*_i$, *i.e.* for $\lambda_{\max}/\lambda_{\min} \geq 2$ and for $\theta \leq \theta_2 = \sin^{-1}(\lambda_{\max}D^*/4)$.

When $d^*_e < 2d^*_i$, we may obtain a lower limit from the fact that the number density for Laue reflections is never less than Q times the number density for accessible RLPs. However, we can get a more precise estimate by comparing (3.3) for rays with (3.2) for RLPs at θ_2 where $d^*_e = D^*$ and $d^*_i = D^*/2$. Corresponding to the factor $Qd_e^{*3} = QD^{*3}$ in (3.3), there is then in (3.2) a factor $D^{*3}[1-(1/2)^3] = (7/8)D^{*3}$. Thus at θ_2 the ratio between rays and RLPs is $(8/7)Q = 0{\cdot}951$. When $d^*_e < 2d^*_i$, the ratio will be nearer unity. Hence whenever $d^*_e < 2d^*_i$, the number of Laue reflections per unit area of a planar detector may be written

$$\frac{1}{CF^2}\,\frac{q}{12V^*}\,[d_e^{*3} - d_i^{*3}]\,\frac{\cos^3 2\theta}{\sin\theta}, \qquad (3.4)$$

where $0{\cdot}951 \leq q \leq 1{\cdot}000$. This estimate is surely adequate for most practical purposes; accurate values may be obtained by examination of the volumes $V(m, n)$ described by CHM1.

As with RLPs, for an averaged orientation of the crystal, the number density of Laue reflections per unit area of the detector will be maximum for $\theta = \theta_c$, where from (3.3) it has the value

$$\frac{1}{CF^2}\,\frac{Q}{6V^*}\,\frac{D^{*2}}{\lambda_{\min}}\cos^3 2\theta_c \qquad (3.5)$$

and is independent of $\lambda_{\max}$. Equations (3.3) and (3.4) provide the explanation for the observation of § 2 that the density rises rapidly from the centre to a maximum and then decreases slowly towards the edge of the plate. Further they show the expected, and practically most important, features that the density is everywhere inversely proportional to CF^2 and to V^*; the maximum density is proportional to $D^{*2}/\lambda_{\min}$.

Results for spherical detectors of radius CF may be obtained by omitting the factor $\cos^3 2\theta$ in (3.2)–(3.5).

Equation (3.4) for the number of Laue reflections per unit area can also be interpreted in a form useful for narrower band passes, *i.e.* when $\lambda_{\max} < 2\lambda_{\min}$. With the substitution $d^* = 2\sin\theta/\lambda$, (3.4) becomes

$$\frac{1}{CF^2}\,\frac{2q}{3V^*}\left[\frac{1}{\lambda^3} - \frac{1}{\lambda^3_{\max}}\right]\sin^2\theta\cos^3 2\theta, \qquad (3.6)$$

where $\lambda = \lambda_{\min}$ for $\theta \leq \theta_c$ and $\lambda = 2\sin\theta/D^*$ for $\theta > \theta_c$. If we compare two cases (a) $\lambda_{\max} = 1{\cdot}1\lambda_{\min}$ (q is then close to $1{\cdot}00$) and (b) $\lambda_{\max} = 2\lambda_{\min}$ ($q = 0{\cdot}951$), we note from (1.2) that the total number of RLPs for case (a) is only 10% of that for (b). Nevertheless throughout the range $0 < \theta \leq \theta_c$ the density for (a) is 30% of that for (b). This relative enhancement is because the limit θ_m is much closer to θ_c in case (a).

3.3. *Wavelength distribution*

What is the wavelength distribution for the reflections appearing in a small area on the detector? Since reflections of multiple order involve several wavelengths, this question can be considered only in terms of the statistical distribution of wavelengths for RLPs. To obtain the distribution, we simply set $d^*_e = 2\sin\theta/\lambda$ and $d^*_i = 2\sin\theta/(\lambda + \mathrm{d}\lambda)$ in (3.2). We then find, effectively for an averaged orientation of the crystal, that the number of RLPs with wavelengths in the range $\lambda, \lambda + \mathrm{d}\lambda$ mapped per unit area of the detector is

$$\frac{1}{CF^2}\,\frac{2}{V^*}\sin^2\theta\cos^3 2\theta\,\frac{\mathrm{d}\lambda}{\lambda^4}. \qquad (3.7)$$

Thus, for a given value of θ, the wavelength probability distribution is inversely proportional to λ^4. The wavelength range is determined by the actual d^*_e and d^*_i at the given θ and extends from $\lambda_{\min}$ or $\lambda = 2\sin\theta/D^*$, whichever is larger, up to $\lambda_{\max}$ (Fig. 5).

We note that all RLPs with λ near $\lambda_{\min}$ are recorded with θ values lying between 0 and θ_c and are therefore found in the centre of the Laue pattern. However, reflections with λ near $\lambda_{\max}$ are recorded with all possible θ values between 0 and θ_m. Nevertheless, the θ range 0 to θ_c records only a small fraction $(\lambda_{\min}/\lambda_{\max})^4$ of the RLPs stimulated by $\lambda_{\max}$. Thus, statistically, the central region of a Laue pattern consists predominantly of reflections stimulated by short wavelengths. This is illustrated, for example, by Fig. 6 which colour codes RLPs by wavelength in a simulated diffraction pattern.

Table 1. *The variation of mean* λ *and* $\sigma(\lambda)$ *with* θ

θ	Fraction recorded	L (λ_{max}/λ_e)	Range of λ/λ_{min}	$\langle\lambda\rangle/\lambda_{min}$	$\sigma(\lambda)/\lambda_{min}$	$\lambda_{med}/\lambda_{min}$
3·44°	0·066	6	1–6	1·47	0·60	1·26
6·89°	0·328	3	2–6	2·77	0·80	2·49
10·37°	0·575	2	3–6	3·86	0·74	3·63
13·89°	0·788	1·5	4–6	4·74	0·55	4·62
17·46°	0·940	1·2	5–6	5·44	0·28	5·41
21·10°	1·000	1	(6–6)	(6·00)	(0)	(6·00)

Notes

1. The calculations assume $\lambda_{max}/\lambda_{min} = 6$ and $\lambda_{max}D^* = 0{\cdot}72$.
2. The second column gives the fraction of all accessible RLPs which are recorded between $\theta = 0$ and the θ of column 1.
3. The top line of the table is for $\theta = \theta_c = \sin^{-1}(\lambda_{min}D^*/2) = 3{\cdot}44°$. For any $\theta < \theta_c$, the range of λ is the same as for $\theta = \theta_c$; hence $\langle\lambda\rangle$ and λ_{med} are also the same.

As a further analysis, we note that the mean wavelength $\langle\lambda\rangle$ at any θ can be calculated as

$$\langle\lambda\rangle = \lambda_e(3/2)[(L^2+L)/(L^2+L+1)], \tag{3.8}$$

where $L = \lambda_{max}/\lambda_e$ and λ_e is the larger of λ_{min} and $2\sin\theta/D^*$ (*i.e.* λ_e is the value of λ on the surface S_e). The standard deviation of the wavelength distribution is $\sigma = (\langle\lambda^2\rangle - \langle\lambda\rangle^2)^{1/2}$, where

$$\langle\lambda^2\rangle = \lambda_e^2(3L^2)/(L^2+L+1). \tag{3.9}$$

The distribution is obviously skew, with median λ_{med} less than $\langle\lambda\rangle$ and

$$\lambda_{med} = \lambda_e[(2L^3)/(L^3+1)]^{1/3}. \tag{3.10}$$

For an example with $\lambda_{max} = 6\lambda_{min}$ and $\lambda_{max}D^* = 0{\cdot}72$, Fig. 4 and Table 1 show how $\langle\lambda\rangle$ increases with θ. Note that $\langle\lambda\rangle$ lies towards the lower end of the local wavelength range. Also shown in Table 1 are $\sigma(\lambda)$, λ_{med} and the fraction of all RLPs recorded by a given θ. Fig. 5 shows the wavelength probability distributions (3.7) at the same values of θ as used in Table 1.

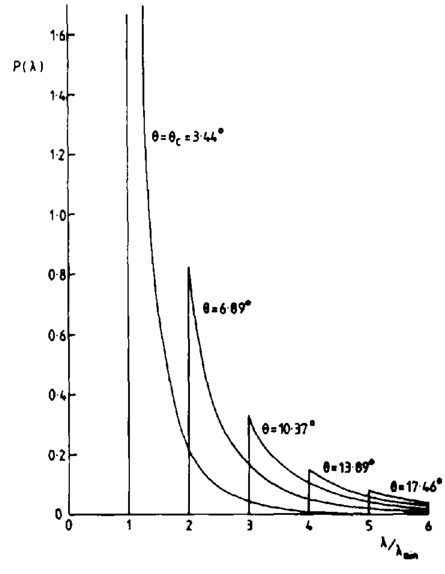

Fig. 5. Wavelength probability distributions $P(\lambda)$ at various θ. The parameters used are $\lambda_{max}/\lambda_{min} = 6$ and $\lambda_{min}D^* = 0{\cdot}12$, so that $\theta_c = \sin^{-1}(0{\cdot}12/2) = 3{\cdot}44°$. Distributions are shown for those θ where $\sin\theta = n\sin\theta_c$ ($n = 1, \ldots, 5$). $\theta = 10{\cdot}37°$ also corresponds to $\theta_2 = \sin^{-1}(\lambda_{max}D^*/4)$. $P(\lambda)$ is on an arbitrary scale and is proportional to $\sin^2\theta\cos^3 2\theta(\lambda_{min}/\lambda)^4$.

Adjacent reflections of spacings d_1^* and d_2^* with nearly the same value of θ may be stimulated by very different wavelengths λ_1 and λ_2 [see Fig. 2(*c*), Clifton *et al.*, 1985]. Since $2\sin\theta_1 = \lambda_1 d_1^*$ and $2\sin\theta_2 = \lambda_2 d_2^*$, when $\theta_1 \simeq \theta_2$ we have $\lambda_1 d_1^* \simeq \lambda_2 d_2^*$. If both reflections are single, then $0{\cdot}5 \leq d_2^*/d_1^* \leq 2$ and consequently $0{\cdot}5 \leq \lambda_1/\lambda_2 \leq 2$. If λ_2 is the shorter wavelength, λ_1 cannot exceed $2\lambda_2$. Conversely, adjacent reflections may be stimulated by exactly the same wavelength when $d_1^* \simeq d_2^*$ and both reflections lie on the same Ewald sphere.

3.4. *Laue patterns further examined*

We now examine some further simulations of Laue patterns in the light of the preceding analysis of the orientation-averaged radial density distribution.

Fig. 7 shows the Laue pattern for pea lectin when the incident beam is along **c** (PL 0° orientation) and the crystal-to-plate distance is 64 mm. The spot pattern has very approximate tetragonal symmetry as $a^* = 0{\cdot}01971$ and $b^* = 0{\cdot}01635$ Å^{-1} have similar values. Thus the families of conics for the $[0kl]$ and $[h0l]$ zones are both visually apparent. In the inner part of the pattern the coarsely averaged density has a very rough circular symmetry and it clearly reaches a maximum at θ_c in accordance with (3.4).

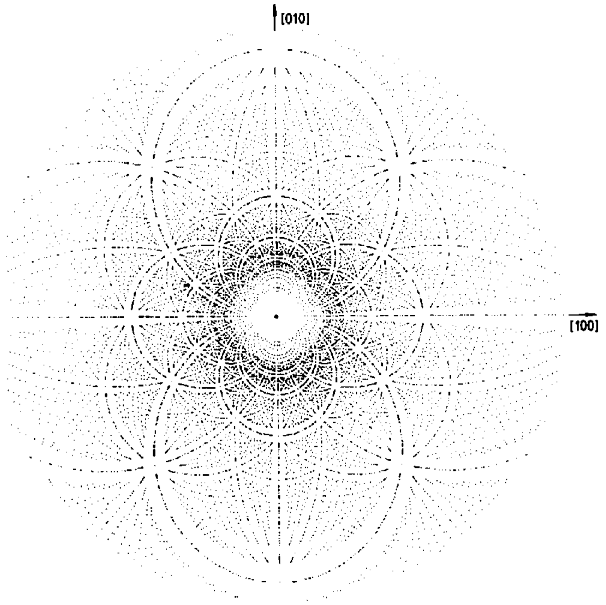

Fig. 7. Computer simulation of Laue pattern for pea lectin. PL 0° orientation, incident beam along **c**. Crystal-to-plate distance: 64 mm.

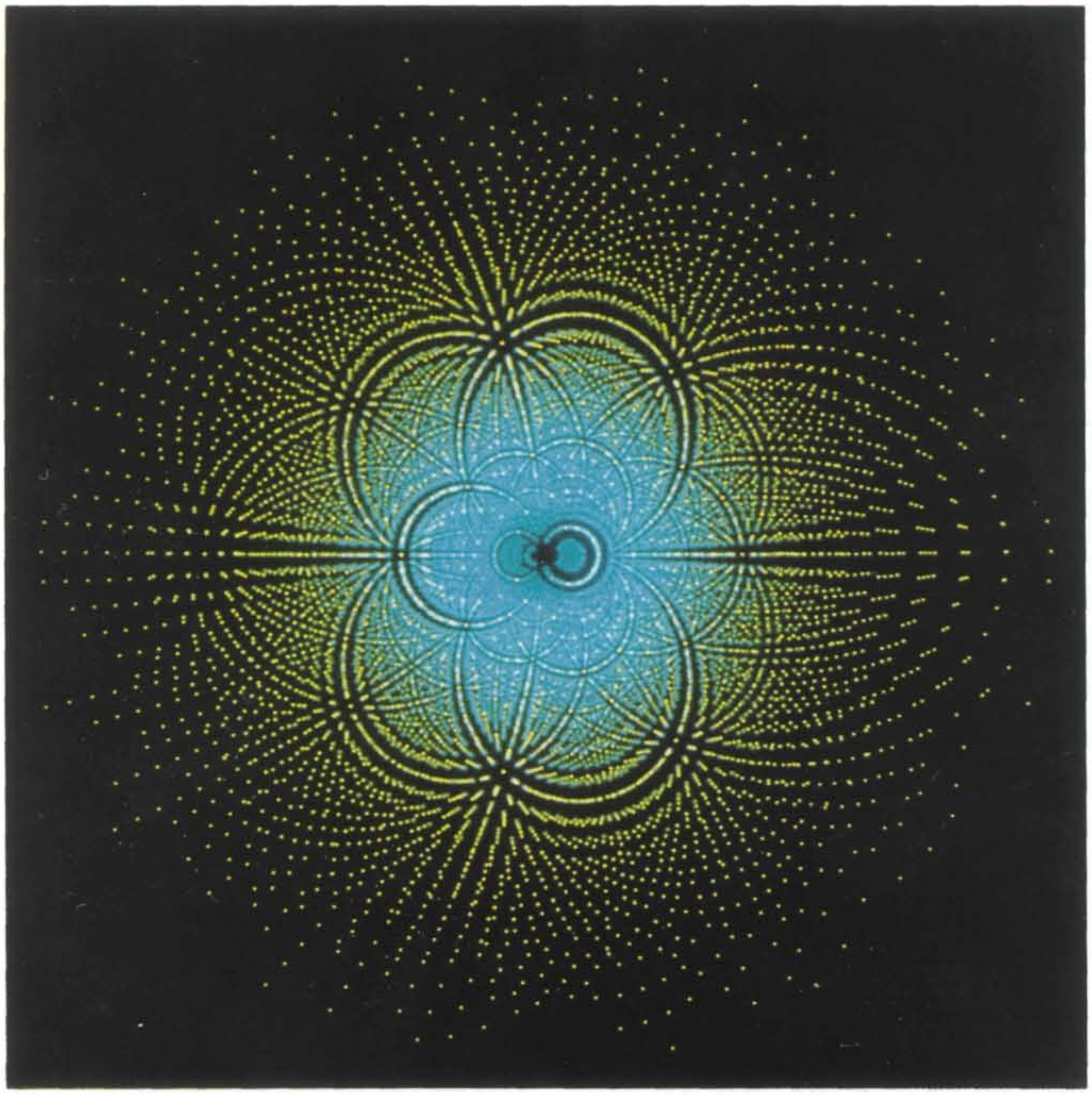

Fig. 6. Computer simulation of Laue pattern for pea lectin, colour coded for wavelength. The spot colours progress from blue for short wavelengths to red for long wavelengths. Multiple-order energy-overlap spots are colour coded according to their longest-wavelength component. Wavelength bins have end points at $(0{\cdot}45+0{\cdot}31n)$ Å for integer $n=0$ to 7. PL 30° orientation and crystal-to-plate distance 34 mm as in Fig. 1(c). This pattern was kindly prepared by Dr P. D. Carr.

With the incident beam still along **c** (PL 0° orientation), Figs. 8(*a*), (*b*) and (*c*) for distances of 95, 64 and 34 mm show only those spots which are involved in spatial overlaps, here defined as spots whose centre-to-centre distance is 0·35 mm or less. The coarse-density maximum at θ_c can be very clearly seen at 34 mm, and is also apparent at 64 mm, but it has been lost at 95 mm. Evidently a large number of spots will be unmeasurable due to spatial overlaps at 34 mm.

Table 2 shows the statistics for Laue patterns (beam along **c**) as a function of crystal-to-plate distance when the plate acceptance radius is held constant at 59·3 mm. It can be seen that the number of RLPs involved in spatial overlaps (column *C*) rises sharply as the crystal-to-plate distance decreases and this counterbalances the more slowly rising total number of RLPs (column *A*). Thus in the conditions exemplified by Table 2, the number of directly measurable RLPs (column *E*) is a maximum at a distance of about 64 mm.

For the 95 mm distance, where there is no obvious sign of a two-dimensional coarse-density maximum at θ_c, it is clear from Fig. 8(*a*) that the great majority of overlapping spots, involving 1214 RLPs, lie along a relatively small number of conic arcs. These correspond to about 30 zones of low indices. For the 64 mm distance in Fig. 7(*b*), where 3758 RLPs are involved in spatial overlaps, the concentration along arcs is also evident. Careful examination of the 34 mm distance in Fig. 8(*c*), where 10408 RLPs are involved in spatial overlaps, shows that these overlaps also are concentrated along conic arcs, albeit a much larger number of conics.

Thus the practical spatial overlap problem has a one-dimensional character, that of the linear density of spots along arcs. Consequently we now turn to the problem of the distribution of spots along the arcs of zone conics.

4. Zones and cones

4.1. *Background*

A central plane of RLPs, or *zone*, may be defined by the origin and two other points (h_1, k_1, l_1) and (h_2, k_2, l_2). Any other RLP in this plane satisfies

$$hu + kv + lw = 0,$$

where $u = k_1l_2 - k_2l_1$, $v = l_1h_2 - l_2h_1$, $w = h_1k_2 - h_2k_1$. The RLPs in this plane form a two-dimensional net whose primitive cells have area $A^*(uvw)$. The normal to this net plane is the line from the origin to the point (u, v, w) in direct space. This is the zone axis $[uvw]$. If $P[uvw]$ is the distance from the origin to the inner point of the row $[uvw]$ in direct space, then

$$P[uvw] = A^*(uvw)/V^* \qquad (4.1)$$

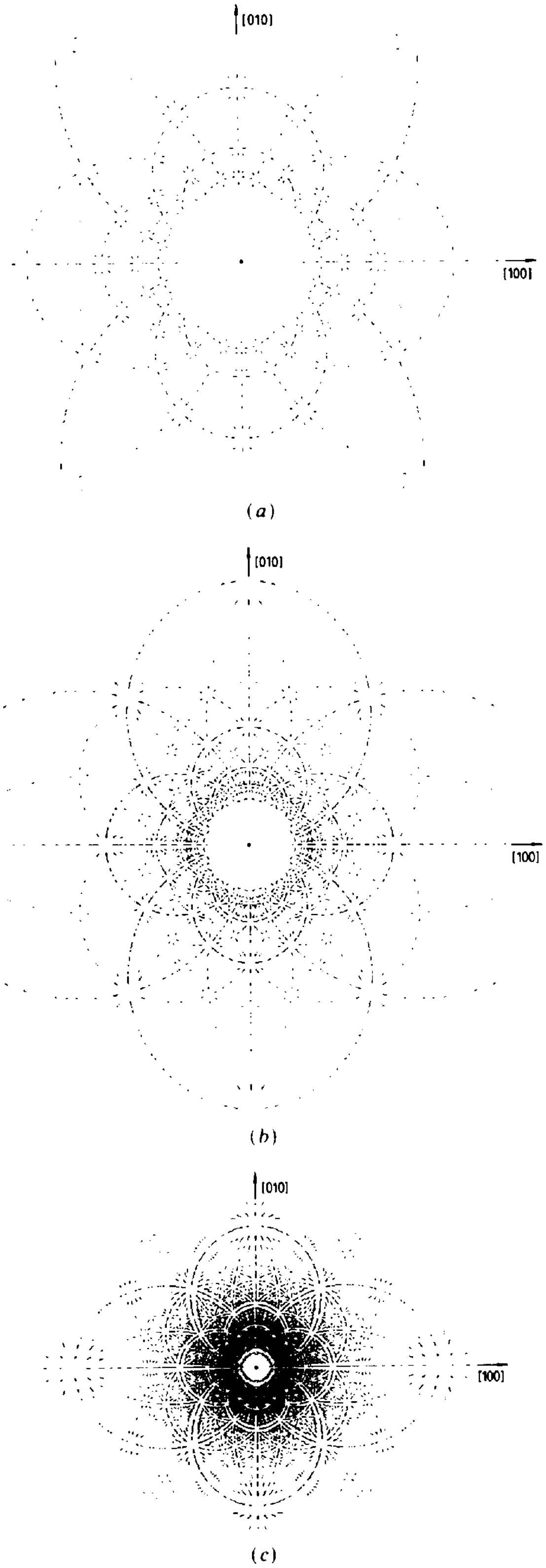

Fig. 8. Computer simulations of Laue patterns for pea lectin, but showing only spots involved in spatial overlaps. PL 0° orientation, incident beam along **c**. Crystal-to-plate distances: (*a*) 95 mm, (*b*) 64 mm, (*c*) 34 mm.

Table 2. *The variation with crystal-to-plate distance of the numbers of Laue spots, RLPs and overlaps*

Crystal-to-plate distance (mm)	Number of Laue spots intercepted by the plate	Number of stimulated RLPs intercepted by the plate	Number of RLPs in energy overlaps	Number of RLPs in spatial overlaps	Number of RLPs in energy and spatial overlaps	Number of RLPs free from energy or spatial overlaps	% of RLPs intercepted and free from overlaps
		A	B	C	D	$E = A - B - C + D$	
120	6826	7894	1848	420	0	5626	35·9
95	8802	10 010	2082	1214	0	6714	42·8
80	10 304	11 564	2184	2152	52	7280	46·5
64	12 046	13 352	2260	3758	236	7570	48·3
50	13 502	14 814	2268	6144	640	7042	44·9
34	14 358	15 670	2268	10 408	1524	4518	28·8

Notes

1. Total number of stimulated RLPs 15 670 (see Note 4).
2. Spatial overlap criterion used was spot centre-to-centre of 0·35 mm or less.
3. Perfectly set crystal of pea lectin, incident beam along **c**, PL 0° orientation, $a^* = 0{\cdot}01971$, $b^* = 0{\cdot}01635$, $c^* = 0{\cdot}00732$ Å^{-1}; $\lambda_{\min} = 0{\cdot}45$, $\lambda_{\max} = 2{\cdot}6$ Å, $D^* = 1/d_{\min} = 1/2{\cdot}6$ Å^{-1}; plate radius 59·3 mm.
4. The 34 mm distance was set by the need for a 59·3 mm radius plate to accept the maximum stimulated Bragg angle $\theta_m = \sin^{-1}(\lambda_{\max} D^*/2) = 30{\cdot}0°$. The 95 mm distance was that chosen in the original experiments of Helliwell (1984, 1985).

(*cf.* $\mathbf{a} = \mathbf{b}^* \wedge \mathbf{c}^*/V^*$). As an example, the RLPs (1, 3, 3) and (6, −5, −5) yield $u = 0$, $v = 23$, $w = -23$, so the zone axis is $[01\bar{1}]$. The RLPs in this zone plane satisfy $k - l = 0$, and hence have indices of the type *hkk*.

4.2. *Conics*

Any net plane of RLPs passing through the origin has an associated zone axis [*uvw*]. On a flat detector the reflections from the accessible RLPs of this plane are recorded in the Laue method as a series of spots lying on a conic. These conics have been known from the earliest days of X-ray crystallography. That the loci are conics may be proved from the diffraction construction.

All RLPs on any ray reflect the incident beam at the same Bragg angle θ and same azimuth β. Accordingly the direction of the diffracted beam is determined only by the orientation of the ray and we may find its direction by using the Ewald construction with an arbitrary wavelength. A zone plane, which contains many rays, intersects an Ewald sphere of arbitrary radius in a circle. The sphere centre C and the circle define a right-circular cone, whose axis is parallel to the zone axis [*uvw*], Fig. 9(*a*). By the Ewald construction, the directions of the diffracted beams lie on the surface of this cone. Any plane section of such a cone is a conic section: ellipse, parabola or hyperbola. All conics pass through F, the point at which the incident beam meets the plate.

Let ψ be the cone half-angle, *i.e.* the angle between the zone axis and the incident beam. If the detector is normal to the incident beam, the angle between the detector normal and the cone axis is also ψ. The conic is an ellipse, parabola or hyperbola according as $\psi < \pi/4$, $\psi = \pi/4$ or $\psi > \pi/4$. Further details of conic geometry are given in Appendix 1.

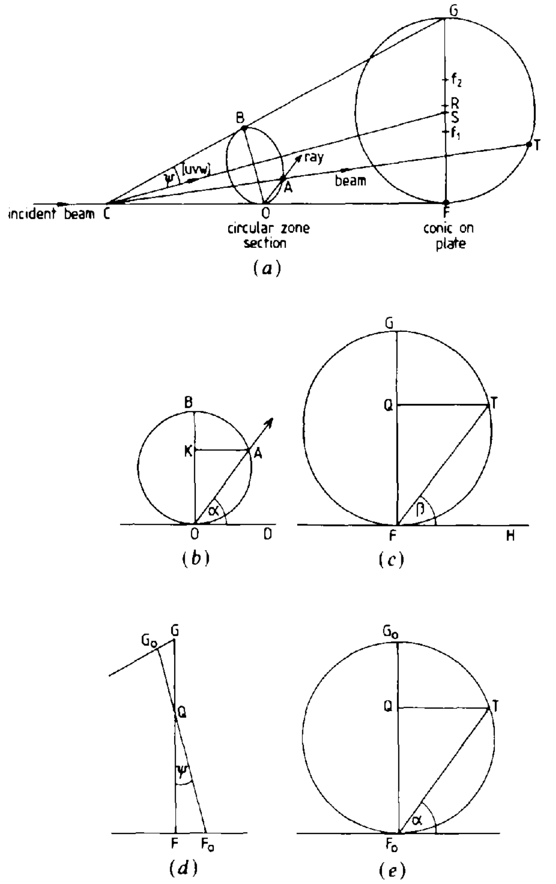

Fig. 9. Diffraction geometry. C is centre of Ewald sphere of arbitrary radius. The zone axis [*uvw*] makes an angle ψ with the incident beam, which meets the detector at F. (*a*) Zone conic formed on detector by circular zone section from Ewald sphere. R is conic centre; f_1, f_2 foci. (*b*) Ray OA in zone plane (corresponding to beam CT); O is origin of reciprocal lattice. (*c*) Normal view of conic on detector. (*d*) Side view of tilted detector. (*e*) Normal view of tilted detector.

5. Rays and beams

5.1. *Azimuthal coordinates*

As in CHM1 we use the word *ray* to denote a line in the reciprocal lattice passing through the origin. We use the word *beam* to denote the direction of a diffracted X-ray beam. We now consider how rays and beams are related and in particular how the small angle $\delta\alpha$ between two neighbouring rays is related to the small angle $\delta\gamma$ between the corresponding neighbouring beams.

Fig. 9(*b*) shows a normal view of the circular section cut by the zone plane from an Ewald sphere of arbitrary radius $1/\lambda$ and Fig. 9(*c*) shows a normal view of the corresponding conic (in this case an ellipse) on the detector. The directions of the two normals to Figs. 9(*b*) and (*c*) differ by the cone half-angle ψ. Let the line of intersection of the zone plane with the origin tangent plane be OD. Let FH be the corresponding parallel line on the detector, so that $\angle TFH=\beta$ measures the azimuth of the diffracted beam CAT. If in the circular zone section $\alpha=\angle AOD$, then $OA=OB\sin\alpha$, but $OA=2\sin\theta/\lambda$ and $OB=2\sin\psi/\lambda$. Hence

$$\sin\theta=\sin\psi\sin\alpha, \tag{5.1}$$

which relates the angular position of a ray in a zone plane to the zone inclination and the Bragg angle of the diffracted beam.

The azimuthal coordinate β of the point T on the detector, Fig. 9(*c*), can be expressed in terms of the corresponding coordinate α of the point A in the zone, Fig. 9(*b*). If QT is the normal from T to the major axis of the conic, suppose the detector to be tilted by ψ about QT as axis so that it becomes parallel to the zone plane, Fig. 9(*d*). The point of incidence of the direct beam on the plate is then F_0 and $\angle F_0QF=\psi$. The conic formed on the detector by the diffraction cone is now a circle with $\beta_0=\alpha$, Fig. 9(*e*). Since the tilted detector is parallel to the zone plane, the triangles OKA and F_0QT are similar and

$$\tan\alpha=OK/KA=F_0Q/QT.$$

But $F_0Q=FQ/\cos\psi$, so that from Fig. 9(*c*)

$$\tan\beta=FQ/QT=F_0Q\cos\psi/QT.$$

Hence

$$\tan\beta=\cos\psi\tan\alpha. \tag{5.2}$$

5.2. *Angular separations*

If in the zone plane, Fig. 9(*b*), OA and OA' are neighbouring rays separated by an angle $\delta\alpha$, then the corresponding diffracted beams CT and CT' are separated by an angle

$$\delta\gamma=\angle TCT'=\angle ACA'=AA'/(1/\lambda),$$

since $AC=A'C=1/\lambda$. Since $\delta\alpha$ is small, AA' is effectively tangential to the circle at A and AA' makes an angle α with OA. Consequently,

$$\begin{aligned}AA'&=OA\delta\alpha/\sin\alpha\\&=(2\sin\theta/\lambda)\delta\alpha/\sin\alpha=2\sin\psi\,\delta\alpha/\lambda.\end{aligned}$$

Hence,

$$\delta\gamma=2\sin\psi\,\delta\alpha, \tag{5.3}$$

which is the general relation between the angle $\delta\alpha$ between two neighbouring rays in reciprocal space and the angle $\delta\gamma$ between the corresponding diffracted beams.

A small solid angle $\delta\Omega_\alpha$ in reciprocal space may be regarded as formed from two orthogonal elements $\delta\alpha_a$ and $\delta\alpha_b$, where $\delta\alpha_a$ is a small angular displacement from a reference ray in the plane a of the incident beam and the reference ray and $\delta\alpha_b$ is a small angular displacement in a plane b perpendicular to plane a. If the reference ray has Bragg angle θ, the zone plane a has $\psi=\pi/2$ and the zone plane b has $\psi=\theta$. The corresponding displacements $\delta\gamma_a$ and $\delta\gamma_b$ of the diffracted beams are also orthogonal. Hence

$$\begin{aligned}\delta\gamma_a\delta\gamma_b&=2\sin(\pi/2)\delta\alpha_a 2\sin\theta\,\delta\alpha_b\\&=4\sin\theta\,\delta\alpha_a\delta\alpha_b,\end{aligned}$$

or in terms of solid angles $\delta\Omega_\gamma$ and $\delta\Omega_\alpha$ measured respectively from C and O

$$\delta\Omega_\gamma=4\sin\theta\,\delta\Omega_\alpha. \tag{5.4}$$

6. Ray separations

We now derive expressions for the angular separations between adjacent rays passing through RLPs of the accessible region. The method used depends on the general properties of lattices and in part develops ideas contained in Bravais's classic memoir of 1850 (see translation: Bravais, 1949). The general properties of lattices apply equally to the direct lattice and the reciprocal lattice. The latter is discussed by Bravais as the *polar lattice*; it differs from the reciprocal lattice by a scale factor (see also Cruickshank, 1991).

6.1. *Plane nets*

A cone of diffracted beams is generated by the RLPs lying in the zone plane perpendicular to the zone axis [*uvw*]. These RLPs are part of a two-dimensional net of points. Base axes for this net can be chosen in many ways. Let A_1 and A_2 be the inner points of two rays (central rows). Bravais defines the rays OA_1 and OA_2 as *conjugate* when no RLP falls within the parallelogram defined by OA_1 and OA_2. Such a parallelogram is then a generating parallelogram of the net. A theorem of Bravais shows that the generating parallelograms of a net all have the same area, whatever conjugate rays are chosen.

Suppose, as in part of the discussion of § 3.2 on Laue reflection distributions that $\lambda_{\max}/\lambda_{\min} \geq 2$ and that we consider the region where $\theta \leq \theta_2 = \sin^{-1}(\lambda_{\max} D^*/4)$, so that $d_e^* \geq 2d_i^*$ on every ray. In this region the angular positions of the accessible rays are determined only by the external surface S_e.

Consider two adjacent rays of the accessible region of the net whose inner points A_1 and A_2 lie on or within S_e. These two inner points and the origin define a parallelogram, whose fourth vertex A_4 must lie outside the accessible region, since otherwise OA_1 and OA_2 would not be adjacent accessible rays. Since the surface S_e is convex, no accessible RLPs lie within the triangle OA_1A_2 and because any net has a centre of symmetry at the centre of every parallelogram, no RLPs can lie within the triangle $A_4A_2A_1$. Accordingly there are no RLPs inside the parallelogram $OA_1A_4A_2$ and consequently the two rays $OA_1 = \mathbf{d}_1^*$ and $OA_2 = \mathbf{d}_2^*$ are conjugate in the sense of Bravais.

Thus $\mathbf{d}_1^*$ and $\mathbf{d}_2^*$ form a generating parallelogram (unit cell) in the $[uvw]$ plane, whose area $A^*(uvw)$ is the same for all adjacent pairs $\mathbf{d}_i^*$, $\mathbf{d}_j^*$ of the accessible region of the plane. Thus $A^*(uvw)$ is also the area of the conventional primitive cell for this reciprocal net plane.

The angle α_{12} between adjacent rays is given by

$$\alpha_{12} = \sin^{-1}(A^*/d_1^* d_2^*) \tag{6.1}$$

or, since α_{12} is small for adjacent rays, it is closely given by

$$\alpha_{12} = A^*/(d_1^* d_2^*). \tag{6.2}$$

Also by (4.1), $A^*(uvw) = P[uvw]V^* = P[uvw]/V$ where $P[uvw]$ is the distance from the origin to the inner point of the $[uvw]$ zone axis and V is the direct-space unit-cell volume. Hence α_{12} may also be written

$$\alpha_{12} = P[uvw]/d_1^* d_2^* V. \tag{6.3}$$

Equations (6.2) and (6.3) for the angle between adjacent rays are valid when $\theta \leq \theta_2$. When $\theta > \theta_2$ some rays whose inner points are within S_e will have no accessible RLPs between S_e and S_i, and these rays will be missing in the Laue pattern. Thus for $\theta > \theta_2$, (6.2) must be replaced by

$$\alpha_{12} = (r+1)A^*/d_1^* d_2^*,$$

where r is the number of missing rays.

6.2. *Space lattices*

Consider now three non-coplanar rays OA_1, OA_2, OA_3, where A_1, A_2, A_3 are inner points. If the parallelepiped defined by these rays contains no RLPs within it or on its lateral faces, the three rays are called *conjugate* by Bravais and the parallelepiped is a generating parallelepiped of the reciprocal lattice. Bravais showed that the generating parallelepipeds of a lattice all have the same volume. In our problem this volume is V^*, the conventional primitive reciprocal unit-cell volume. By a standard formula

$$V^* = d_1^* d_2^* d_3^* [1 - \cos^2\alpha_{23} - \cos^2\alpha_{31} - \cos^2\alpha_{12} + 2\cos\alpha_{23}\cos\alpha_{31}\cos\alpha_{12}]^{1/2},$$

where α_{23}, α_{31}, α_{12} are the inter-ray angles. If the inter-ray angles are small,

$$\begin{aligned}
&[1 - \cos^2\alpha_{23} - \ldots]^{1/2} \\
&\quad = \tfrac{1}{2}[2\alpha_{31}^2\alpha_{12}^2 + 2\alpha_{12}^2\alpha_{23}^2 \\
&\qquad + 2\alpha_{23}^2\alpha_{31}^2 - \alpha_{23}^4 - \alpha_{31}^4 - \alpha_{12}^4]^{1/2} \\
&\quad = 2[s(s-\alpha_{23})(s-\alpha_{31})(s-\alpha_{12})]^{1/2} \\
&\quad = 2\alpha_{123},
\end{aligned} \tag{6.4}$$

where $s = (\alpha_{23} + \alpha_{31} + \alpha_{12})/2$ and α_{123} is the solid angle defined by the three rays (*i.e.* the area in steradians of the spherical triangle defined by the three rays). Accordingly

$$\alpha_{123} = \tfrac{1}{2}\frac{V^*}{d_1^* d_2^* d_3^*}, \tag{6.5}$$

provided the three rays are conjugate and the angles between them are small.

We may describe three non-coplanar rays as mutually adjacent if each pair of rays forms an adjacent pair in the accessible region of the zone defined by the pair. We now ask, for $\theta < \theta_2$, whether three such non-coplanar mutually adjacent rays are conjugate if the spherical triangle corresponding to α_{123} has no other accessible rays within it? The answer is: often, but not necessarily. The requirement that the three rays be conjugate is stronger than a requirement that the rays be conjugate in pairs. If the rays are conjugate in pairs, there are no RLPs on any of the faces of the parallelepiped, but nothing is implied about the interior. Since S_e is convex the tetrahedron $OA_1A_2A_3$ contains no inner points within it as otherwise the corresponding rays would appear within the solid angle α_{123}. However, this tetrahedron and the inverse one at the far vertex of the parallelepiped occupy only 2/6 of the volume of the parallelepiped and the reciprocal lattice may have inner points outside S_e but within the parallelepiped. Thus the solid angle formed by three mutually adjacent rays may be an integral multiple of the value given by (6.5). This multiple is equal to the determinant of the indices of the inner points of the rays.

The spatial overlap problem is concerned with small values of the inter-ray angles $\alpha_{12}, \ldots$. Can two or three of the inter-ray angles involved in α_{123} be simultaneously very small? If the zones corresponding to α_{23} and α_{31} are perpendicular, $\alpha_{123}=\frac{1}{2}\alpha_{23}\alpha_{31}$. If for simplicity we consider a cubic cell of side a^* and all $d^*\simeq D^*$, then $V^*=a^{*3}$ and the smallest $A^*=a^{*2}$. Hence the smallest inter-ray angle $\alpha_{23}\simeq a^{*2}/D^{*2}$, but

$$\alpha_{123}\simeq\tfrac{1}{2}a^{*3}/D^{*3}\simeq\alpha_{23}\tfrac{1}{2}a^*/D^*.$$

Thus

$$\alpha_{31}\simeq a^*/D^*\simeq a^{*2}/(D^*a^*),$$

which is D^*/a^* times the smallest angle α_{23}.

Accordingly when three mutually adjacent conjugate rays are considered, only one of the inter-ray angles can be very small. The other two angles must be substantially larger. This explains the observation that the spatial overlaps in Laue patterns at moderate crystal-to-plate distances do not form two-dimensionally overcrowded clumps but cluster along the arcs of zones.

6.3. *Example*

To illustrate (6.2), $\alpha_{12}=A^*/(d_1^*d_2^*)$ for ray separations when $\theta<\theta_2$, consider the zone net in Fig. 10. For simplicity the lattice has been taken as square and the external boundary S_e of the accessible region has been taken as a circle of radius D^*. Since we are considering ray separations an inner boundary S_i has been omitted, because no rays with inner points inside S_e can be lost when $\theta<\theta_2$.

The diagram illustrates theorem 2 of CHM1 that rays of multiplicity n within S_e have their inner points at radii between D^*/n and $D^*/(n+1)$. As can be seen, the inner (and sole) points of all singles have radii $\geq D^*/2$, while the inner points of all doubles lie between $D^*/2$ and $D^*/3$. The ray at the bottom of Fig. 10 through the RLP (1, 0) has multiplicity 13, and has a large angular separation 4·76° from its neighbour (12, 1), which is a single. (12, 1) is separated from (11, 1) by a small angle 0·43° and the gap between successive singles increases slowly to 1·01° between (8, 1) and (7, 1). The ray through (6, 1) is a double and makes angles 1·33° with (7, 1) and 0·84° with (11, 2). Then comes the double (5, 1) and a single (9, 2), followed by a triple (4, 1), three singles (11, 3), (7, 2), (10, 3) and a quadruple (3, 1). After two singles, a double (5, 2) and four singles, the quintuple (2, 1) is reached and this makes the relatively large angles 2·13 and 2·04° with its adjacent singles.

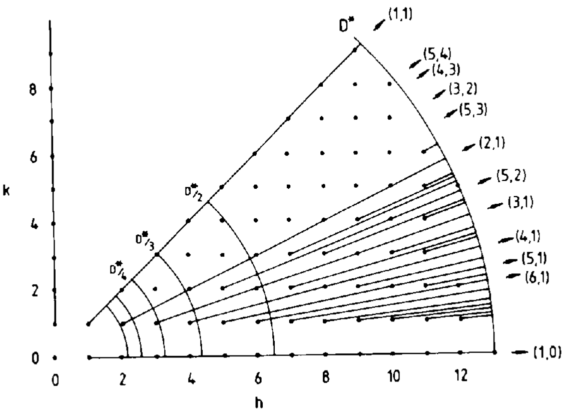

Fig. 10. Rays in a zone net. Square lattice with $D^*=13a^*$ so that $h_{\max}=13$. Rays of multiplicity n have their inner points at radii between D^*/n and $D^*/(n+1)$. Doubles and higher multiples are marked by arrows at ends of rays.

6.4. *Analysis and consequences*

In Fig. 10 it can be observed that *no two multiples are adjacent*. This is easily proved to be a general result. For, if two supposedly adjacent n-tuples have as their inner points (1, 0) and (0, 1) in appropriately redefined base axes, the diagonal point (1, 1) lies on the line joining the second-order points (2, 0) and (0, 2) and is thus within the convex boundary S_e. Accordingly an accessible ray lies between the n-tuple rays.

The large angular separation around an n-tuple with high n, also illustrated in Fig. 10, follows immediately from (6.2) for α_{12}, since d_1^* is small when n is large.

Since the inner points of single rays lie between D^* and $D^*/2$ and of n-tuples between D^*/n and $D^*/(n+1)$, it follows by (6.1) that the angle between two single rays lies in the range A^*/D^{*2} to $4A^*/D^{*2}$, while the angle between an n-tuple and a single may be shown to lie in the range nA^*/D^{*2} to $[(n+1)^2/n]A^*/D^{*2}$ (Brooks, Moffat & Cruickshank, 1991).

In Fig. 10, $A^*=a^{*2}$, $h_{\max}=13$ and $D^*=13a^*$, so that $A^*/D^{*2}=1/169$ and $\delta\alpha_{\min}=0{\cdot}34°$. In a version of Fig. 10 extended to the diagonal ray through (1, 1), the actual spread of separations between singles is 0·43 to 1·01°, as compared with the theoretical limits of 0·34 to 1·36°; while the actual spread of separations between doubles and singles is 0·79 to 1·33°, as compared with the theoretical limits of 0·68 to 1·53°.

Both numerical simulations and a simple theory based on random distributions of neighbouring $\mathbf{d}_1^*$ and $\mathbf{d}_2^*$ (Brooks, Moffat & Cruickshank, 1991) show that the statistical distributions of n-tuple:single separations are very skew. For the single:single distribution, shown in Fig. 11, 72% of values are below $2A^*/D^{*2}$, which is the lowest possible value of a double:single separation.

Thus spatial overlaps occur most severely between adjacent single rays.

The average spacing between rays, irrespective of multiplicity, can be estimated as follows. The number of inner points in a sector of angular width $\Delta\alpha$ is $(Q_2/A^*)/(\frac{1}{2}D^{*2}\Delta\alpha)$, where

$$Q_2=(1-1/2^2)(1-1/3^2)(1-1/5^2)\ldots=0{\cdot}608 \quad (6.6)$$

is the probability that a randomly chosen RLP in a two-dimensional net is an inner point (*cf.* the definition of Q in three dimensions, § 1.2). The number of inner points is the same as the number of rays which emerge across the external boundary S_e (provided $d_e^* \geq 2d_1^*$). This boundary subtends the angle $\Delta\alpha$, hence the average angular spacing between rays is

$$\alpha_{\text{avg}} = (2/Q_2)/(A^*/D^{*2}) = 3{\cdot}29 A^*/D^{*2}. \qquad (6.7)$$

This is 3·29 times the minimum possible separation of any two rays. In the example of Fig. 10 α_{avg} was 1·15°, which is satisfactorily close to 3·29 × 0·34° = 1·12°.

7. Beam separations

7.1. *Theory*

The experimental problem about the resolution of adjacent spots concerns interbeam angles, so we now combine two key equations (5.3) and (6.3). The first, $\delta\gamma = 2\sin\psi\,\delta\alpha$, connects the angle $\delta\alpha$ between neighbouring rays with the corresponding angle $\delta\gamma$ between neighbouring beams. The second, $\alpha_{12} = P[uvw]/(d_1^* d_2^* V)$, expresses the angle between adjacent rays in terms of the radii of the inner points of the rays. For the zone in question, their combination gives the angle between adjacent beams as

$$\gamma_{12} = 2P[uvw]\sin\psi/d_1^* d_2^* V. \qquad (7.1)$$

This equation is central to the subsequent analysis.

The minimum possible separation between beams for the zone is

$$\gamma_{\min} = 2P\sin\psi/D^{*2}V, \qquad (7.2)$$

while the average separation between beams when $\theta_c < \theta < \theta_2$ is

$$\gamma_{\text{avg}} = (4/Q_2)P\sin\psi/D^{*2}V. \qquad (7.3)$$

The minimum separation (7.2) applies when both beams are singles with order $n = 1$. When one beam is an n-tuple the minimum separation will be n times as large.

It should be noticed, for a given lattice and for specified rays OA_1 and OA_2, that ψ is the only variable in (7.1) for the interbeam angle. The specification of A_1 and A_2 determines $[uvw]$ and hence P. Nor does γ_{12} depend explicitly on λ, θ or the azimuth. Thus the only direct way to increase a particular γ_{12}, or any other γ_{ij} of the same zone, is to increase $\sin\psi$ by changing the crystal orientation (provided of course that a RLP of each ray remains in the accessible region, which may require $\theta < \theta_2$).

Equation (7.1) offers a simple interpretation of the density of spot spacing along the conics in Laue patterns. $P[uvw]$ is the distance from the origin to the point (u, v, w) of the direct lattice, while ψ is the angle between the zone axis $[uvw]$ and the incident beam. Thus $P\sin\psi$ is the distance from (u, v, w) to the line of the incident beam. Accordingly, in the direct lattice, as shown in Fig. 12, any points (u, v, w) on a cylinder of given radius $P\sin\psi$ define zone conics in the Laue pattern whose arcs have the same average angular beam separation. On a spherical detector of radius CF the spatial separation between spots will be $CF\gamma_{12}$; on a flat plate there will be further factors $1/\cos^2 2\theta$ in the radial direction and $1/\cos 2\theta$ in the orthogonal direction.

7.2. *Examples*

Fig. 2 shows the pea lectin Laue pattern when the incident beam is along the b axis (PL 90° orientation). The conics of some major zones are labelled. The direct-lattice points (1, 0, 0), (1, 1, 0), (1, 2, 0), (1, 3, 0), ... are all at the same distance from the b axis. Hence for all of them $P\sin\psi = a = 51$ Å and the same average interbeam angle is to be expected for the corresponding conics between θ_c and θ_2. It is evident visually in Fig. 2 that the linear density of spots is similar in all these conics.

The zone [210] has $P\sin\psi = 2a = 102$ Å and has its average interbeam separation doubled relative to the $[1v0]$ set.

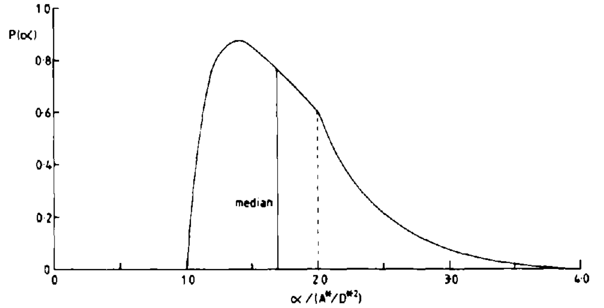

Fig. 11. Single:single probability distribution $P(\alpha)$ for the separation α between adjacent single rays. The mode, median and mean are at $\alpha/(A^*/D^{*2}) = 1{\cdot}396$, 1·687 and 1·778. The smallest possible double:single separation has $\alpha/(A^*/D^{*2}) = 2{\cdot}0$.

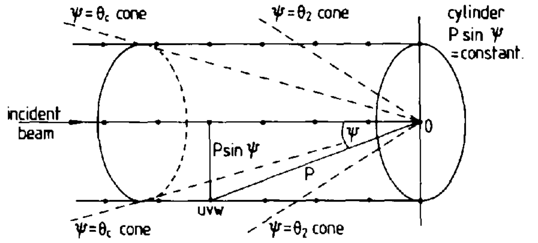

Fig. 12. Direct-lattice points (u, v, w) on cylinder $P\sin\psi =$ constant. The lattice points on the cylinder define zone conics in the Laue pattern, all of which have the same average angular beam separation (for $\theta_c < \theta < \theta_2$).

The zones [001], [011], [021], ... have $P \sin \psi = c = 137$ Å, so that their interbeam separations are still larger. Conversely the gaps bordering their conics are small (being proportional to $1/P$ as will be shown in § 8). It is thus not surprising that the conics of the [$0v1$] set cannot be picked out immediately by eye.

Fig. 13 shows the Laue pattern when the incident beam is along the c axis (PL 0° orientation). Two sets of conics can now be seen easily: the [$10w$] set has $P \sin \psi = a = 51$ Å as for the [$1v0$] set in Fig. 2, and the [$01w$] set has $P \sin \psi = b = 61$ Å. The interbeam spacing in the latter set is slightly greater than in the former set. This may be detected most easily by comparing the [011] and [101] conics which meet at the $11\bar{1}$ nodal point. Through the same nodal point, one can see the straight line of the [$1\bar{1}0$] conic which has $\psi = \pi/2$ and $P \sin \psi = 79$ Å with a larger average spacing between spots.

The [201] conic with $P \sin \psi = 2a = 102$ Å can just be detected, as can, with a little more difficulty, the [021] conic with $P \sin \psi = 2b = 122$ Å.

The PL 30° patterns have already been introduced in § 2, but rather than discuss the full pattern of Fig. 1(a) it will be easier and more pertinent if we analyse Fig. 14 which shows only those spots involved in spatial overlaps closer than 0·35 mm for a crystal-to-plate distance of 95 mm. Some of the main zones are identified and circles have been superposed corresponding to $\theta_c = \sin^{-1}(\lambda_{\min} D^*/2) = 5{\cdot}0°$ and $\theta_2 = \sin^{-1}(\lambda_{\max} D^*/4) = 14{\cdot}5°$. The plate edge occurs at $\theta_{\text{acc}} = 16{\cdot}0°$. In the region between θ_c and θ_2 no rays with inner $d^* \le D^*$ are lost. Thus apart from the flat plate factors, in this region each conic has a constant statistical average density of spots along its arc. Below θ_c the density decreases with d_e^{*2} which is proportional to $\sin^2 \theta$.

Because of the more general orientation of the crystal there is now a variety of values of $P \sin \psi$. The lowest is 15 Å for the [011] conic, which is the very dense ring near the centre. It can be seen that the spacing density along the arc rises as θ increases to θ_c and is then statistically constant. The next lowest $P \sin \psi$ is 22 Å for the [032] conic; however, this is a smaller ellipse which does not reach the θ_c circle and its density is less prominent than the larger [021] ellipse with $P \sin \psi = 38$ Å which reaches almost to θ_2 at the left. It can be seen that the spatial overlap densities of [010] 53 Å, [100] 51 Å and [$\bar{1}11$] 53 Å are very similar. The last two are members of the [$\bar{1}vv$] family, in which by $v = 3$ the spatial overlaps in the [$\bar{1}33$] conic with $P \sin \psi = 69$ Å are only just traceable along the arc. By $v = 5$ only the two points of the conic closest to the $0\bar{1}1$ nodal remain (these points are actually well separated from the nodal by a large gap across the clear area surrounding the [011] conic); [$\bar{1}55$] has $P \sin \psi = 92$ Å.

The essence of the present discussion is as follows. To every conic of spots in a Laue pattern, there corresponds a single point in the direct lattice (the zone axis). The distance of each direct-lattice point from the incident-beam line determines the average spacing of the spots in the corresponding Laue pattern conic.

Some general remarks about the ψ dependence of the accessible areas of zones are given in Appendix 2.

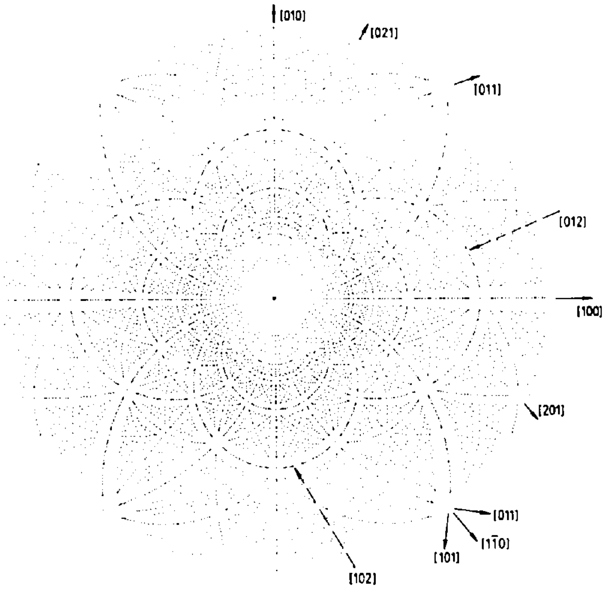

Fig. 13. Computer simulation of Laue pattern for pea lectin. PL 0° orientation, incident beam along **c**. Crystal-to-plate distance: 95 mm.

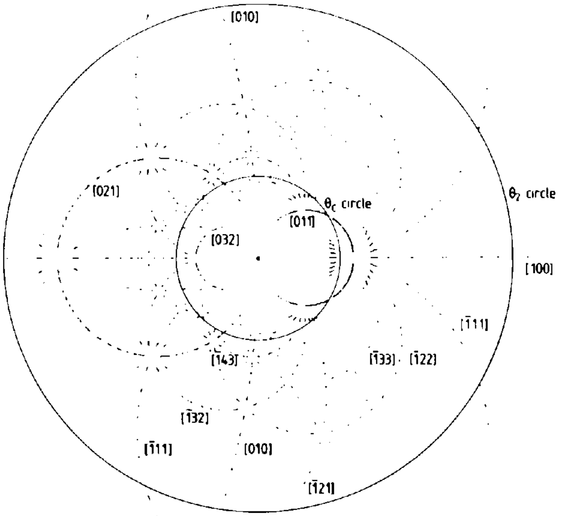

Fig. 14. Computer simulation of Laue pattern for pea lectin, but showing only spots involved in spatial overlaps. PL 30° orientation. Crystal-to-plate distance: 95 mm. The circles have radii corresponding to $\theta_c = \sin^{-1}(\lambda_{\min} D^*/2)$ and $\theta_2 = \sin^{-1}(\lambda_{\max} D^*/4)$.

Table 3. *Variation of optimum crystal-to-plate distance as function of spot-to-spot resolution distance*

Spot-to-spot resolution distance (mm)	Optimum crystal-to-plate distance (mm)	Number of RLPs free from energy or spatial overlaps	% of RLPs intercepted and free from overlaps
0·2	50	10 788	68·8
0·3	60	8532	54·4
0·35	64	7570	48·3
0·4	70	6656	42·5
0·5	80	5174	33·0

Notes

1. Total number of stimulated RLPs 15 670.
2. PL 0° orientation.
3. $\lambda_{\min}$, $\lambda_{\max}$, D^* and plate radius as in Table 2.

Table 4. *Variation of optimum crystal-to-plate distance as function of spot-to-spot resolution distance for doubled cell dimensions*

Spot-to-spot resolution distance (mm)	Optimum crystal-to-plate distance (mm)	Number of RLPs free from energy or spatial overlaps	% of RLPs intercepted and free from overlaps
0·2	100	33 164	26·5
0·3	170	15 878	12·7
0·4	220	8831	7·0
0·5	290	5262	4·2

Notes

1. Total number of stimulated RLPs 125356.
2. PL 0° orientation, with $a^* = 0{\cdot}01971/2$, $b^* = 0{\cdot}01635/2$, $c^* = 0{\cdot}00732/2$ Å^{-1}.
3. $\lambda_{\min}$, $\lambda_{\max}$, D^* and plate radius as in Table 2.

7.3. *Required spot-to-spot resolution capability*

For a given crystal and assuming perfect geometrical conditions, what is the smallest possible angular separation of two diffracted beams? The general equation (7.1) for beam separation is

$$\gamma_{12} = 2\sin\psi\,\alpha_{12} = 2P\sin\psi/(d_1^*d_2^*V).$$

The separation will be smallest when: (i) $P = a_{\min}$, the smallest cell dimension; (ii) the d^* are near their largest value D^*; and (iii) the zone inclination ψ is the smallest compatible with (ii), *i.e.* when $\psi = \theta_c$. Hence, $\sin\psi_c = \sin\theta_c = \lambda_{\min}D^*/2$, so that the smallest possible beam separation is

$$\gamma_{\min} = (a_{\min}\lambda_{\min})/(D^*V). \qquad (7.4)$$

For pea lectin, $P_{\min}\sin\psi_c = 51\sin(5{\cdot}0°) = 4{\cdot}4$ Å and with the parameters used in the simulations of § 2

$$\gamma_{\min} = (51\times 0{\cdot}45)/[(1/2{\cdot}6)\times(51\times 61\times 137)]$$
$$= 1{\cdot}40\times 10^{-4}\text{ rad} = 0{\cdot}0080°.$$

Thus to resolve the smallest possible beam separations from pea lectin, an ability is required to resolve spots 0·14 mm apart on a detector 1 m from the crystal.

This is manifestly an oversevere and unrealistic criterion, for few orientations would lead to any significant number of spots anything like so close. Even for the PL 30° orientation, the closest spots on the [011] conic are three times further apart, $P\sin\psi$ being 15 Å. For a given zone from (6.7), average spot separations are of course 3·29 times the minimum value.

It was evident that spatial overlapping was less acute for the *aligned* PL 0° and PL 90° situations than for PL 30°. In each of the aligned situations the lowest $P\sin\psi$ was 51 Å ($=a$), whereas in PL 30° $P\sin\psi$ dropped to 15 Å. When $P\sin\psi = 51$ Å, and with the parameters used in the simulations of § 2, (7.2) yields

$$\gamma_{\min} = (2P\sin\psi)/(D^{*2}V)$$
$$= (2\times 51)/[(1/2{\cdot}6)^2\times(51\times 61\times 137)]$$
$$= 16{\cdot}2\times 10^{-4}\text{ rad} = 0{\cdot}093°.$$

If the crystal-to-detector distance is 100 mm, the spot-to-spot resolution capability required to avoid *all* spatial overlaps for this orientation is 0·16 mm.

If the requirement is further relaxed to the level of requiring only that all spatial overlaps be avoided in PL 0° for the [20w] zones with $P\sin\psi = 102$ Å, the resolution capability required changes by a factor of 2 to 0·32 mm. This is approximately the situation of PL 0° in Fig. 8(*a*) for which $CF = 95$ mm and the spot-to-spot resolution is 0·35 mm. In this case the seriously overlapped zones are nearly all of the kinds [10w] and [01w]. The data in Table 2 show that 10 010 RLPs are intercepted by the plate at this distance, though 15 670 − 10 010 = 5660 are not intercepted, and that 1214 RLPs are lost due to spatial overlaps. At $CF = 64$ mm fewer RLPs (15 670 − 13 352 = 2318) miss the plate, but the number of spatial overlaps increases to 3758. From Fig. 8(*b*) we see that the number of overlaps in the [10w] and [01w] zones has increased considerably (due to the acceptance limit moving to the right in probability distributions like Fig. 11), and that overlaps are now occurring in zones like [11w].

7.4. *Optimum crystal-to-plate distance*

The computations of Table 2 showed that the 64 mm distance led to the largest number of measurable RLPs. Can such an optimum distance be determined analytically? We have derived a possible formula covering both energy and spatial overlaps, but our examination of it is not yet finished. Here we present simulation results to highlight the effects of different spatial resolutions (Table 3)and the severe impact of larger unit cells (Table 4).

For PL 0° with 0·2 mm resolution the optimum CF distance is 50 mm and 68·8% of the 15 670 stimulated RLPs can be recovered. With 0·5 mm resolution only 33% can be recovered at the optimum 80 mm distance.

The effect of larger unit-cell parameters is dramatic. This can be illustrated (Table 4) by doubling the pea lectin cell dimensions but leaving the plate size and other variables unaltered. The same volume of reciprocal space then contains eight times as many stimulated RLPs, *viz* 125 356 against 15 670. At 0·2 mm resolution, the optimum *CF* distance doubles to 100 mm and 33 164 RLPs can be recovered. However, this represents only 26·5% of the total stimulated RLPs. At 0·4 mm resolution, the optimum *CF* is 220 mm but only 7·0% of RLPs are recovered.

Although spatial overlaps are determined by one-dimensional considerations, some guidance on the choice of crystal-to-plate distance can be obtained from the two-dimensional probability densities derived in § 3. Equation (3.3) gives the number of spots per unit area of plate and, when applied to the pea lectin conditions, shows that even for this unit cell the maximum densities at $\theta = \theta_c$ are 16·0, 4·5 and 2·0 spots mm^{-2} for *CF* 34, 64 and 95 mm. Coupled with a density dependence on θ like Fig. 4, it is thus not surprising that, for *CF* 34 mm, 66% of RLPs are involved in spatial overlaps when the resolution capability is 0·35 mm.

8. Gaps bordering conics

8.1. *Delimiting planes*

A characteristic feature of Laue patterns such as Fig. 1(*a*) is that the conic corresponding to a zone is bordered on both sides by clear regions before other spots are reached. Smooth envelopes may be drawn around the two boundaries of the clear regions, so that no spots lie between these envelopes except the arc of spots belonging to the original zone conic.

The spots on the conic with zone axis $[uvw]$ derive from the RLPs on the zone plane

$$hu + kv + lw = 0.$$

This central plane is bordered, on either side, by the two parallel planes

$$hu + kv + lw = \pm 1.$$

These planes, which are called delimiting planes by Bravais (1949), do not pass through the origin. There are no RLPs between the delimiting planes and the zone plane. Their distance from the zone plane is $1/P[uvw]$.

The envelopes of the clear regions in a Laue pattern correspond to the intersections of the two delimiting planes with the external surface S_e of the accessible region of reciprocal space, *viz* the D^* sphere when $\theta > \theta_c$, or the $1/\lambda_{\min}$ Ewald sphere when $\theta < \theta_c$.

Thus the dimensions of the clear gaps depend on D^* when $\theta > \theta_c$ and on $\lambda_{\min}$ when $\theta < \theta_c$. We shall show also that clear gaps are inversely proportional to P and thus that wide gaps correlate with dense conics. Since good estimates of D^* and $\lambda_{\min}$ are necessary for the processing of data from Laue patterns (Helliwell *et al.*, 1989), we formulate the initial parts of the analysis in terms of the estimation of D^* and $\lambda_{\min}$. The summary comparison of internal conic density and external clear gaps is given in § 8.5.

8.2. *Estimation of D^**

For $\theta > \theta_c$, a simple method of estimating D^* is to examine the clear regions in the direction of the major diameter of a complete ellipse for some prominent zone. The zone inclination ψ must satisfy $\theta_c < \psi < \theta_{\text{acc}}$, where θ_{acc} is the maximum θ accepted by the detector. The major diameter of the ellipse on a planar detector is of length $FG = CF \tan 2\psi$ and the point G arises from a Bragg angle $\theta = \psi$. In this azimuthal direction on the detector, Fig. 15(*a*), the corresponding points G_+ and G_- on the envelopes correspond to Bragg angles $\theta \pm \delta$, where $\delta = \sin^{-1}(1/PD^*)$, since the interplanar spacing is $1/P$ and D^* is the radius of the sphere forming S_e. Thus G_+ and G_- occur on the detector at distances $CF \tan 2(\psi \pm \delta)$ from the detector centre F. Hence the positions of the envelopes give two estimates of δ and thence of D^*.

If δ is small, the angular separation γ_{rad} between the beams striking the detector at G and G_+ (or G_-) is

$$\gamma_{\text{rad}} = 2/PD^*. \qquad (8.1)$$

Also for small γ_{rad}, since $FG = CF \tan 2\psi$,

$$\begin{aligned} GG_+ \simeq GG_- &\simeq CF(\sec^2 2\psi)\gamma_{\text{rad}} \\ &= 2CF \sec^2 2\psi / PD^*. \qquad (8.2) \end{aligned}$$

Hence we may estimate

$$D^* = [2(CF/GG_\pm) \sec^2 2\psi]/P[uvw]. \qquad (8.3)$$

8.3. *Estimation of λ_{min}*

For $\theta < \theta_c$, the corresponding estimate of $\lambda_{\min}$ must be made from a smaller ellipse with $\psi < \theta_c$.

The external surface S_e is now part of the $\lambda_{\min}$ Ewald sphere, which passes through the origin O of the reciprocal lattice. The zone plane *uvw* intersects

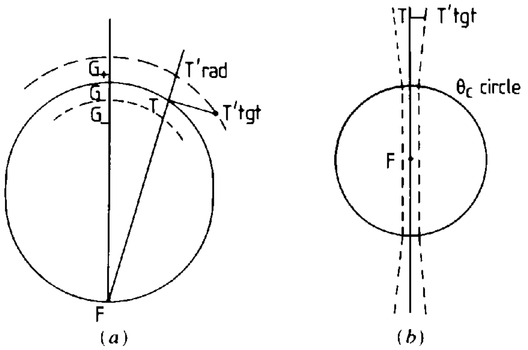

(*a*) (*b*)

Fig. 15. Clear regions bordering zone conics. (*a*) Clear regions around an ellipse. (*b*) Clear regions when $\psi = \pi/2$ and zone conic is a straight line.

S_e in a circle passing through the origin. One or both delimiting planes also intersect S_e in circles, whose centres E_+, E_- lie on the axis of the right-circular cone defined by the zone-plane circle and the centre of the Ewald sphere (Fig. 16). The envelopes for the edges of the accessible regions of the delimiting planes are also defined by right-circular cones.

If ψ_+ and ψ_- are the half-cone angles corresponding to the delimiting planes $hu+kv+lw=\pm 1$, we have

$$CE=\cos\psi/\lambda_{\min};\qquad CE_+=\cos\psi_+/\lambda_{\min};$$
$$CE_-=\cos\psi_-/\lambda_{\min},$$

but

$$CE-CE_+=CE_--CE=1/P[uvw].$$

Hence we may estimate

$$\begin{aligned}\lambda_{\min}&=P[uvw](\cos\psi-\cos\psi_+)\\&=P[uvw](\cos\psi_--\cos\psi).\end{aligned}\qquad(8.4)$$

If the zone axis coincides with the incident-beam direction, then $\psi=0$ and the zone plane is tangential to the $1/\lambda_{\min}$ Ewald sphere. There are no reflections from the zone plane and the Laue pattern has a circular central clear region whose radius is determined by the intersection of the ψ_+ delimiting plane with the Ewald sphere. With $\cos\psi=1$, (8.4) reduces to

$$\begin{aligned}\lambda_{\min}&=P[uvw](1-\cos\psi_+)\\&=2P[uvw]\sin^2(\psi_+/2),\end{aligned}\qquad(8.5)$$

where $\psi_+/2$ is the Bragg angle corresponding to the radius of the clear region. Jeffrey (1958) earlier gave this equation in the form $c=\lambda/(2\sin^2\theta)$, where c is the lattice parameter in the beam direction.

If the differences $\psi_\pm-\psi$ are small in comparison with ψ and $\psi<\theta_c$ so that the ellipse is complete, the angular separation $\gamma_{\rm rad}$ between the beams striking the detector in the radial direction at G and $G_\pm$ is $\gamma_{\rm rad}=\lambda_{\min}/P\sin\psi$. Then

$$\begin{aligned}GG_\pm&=CF(\sec^2 2\psi)\gamma_{\rm rad}\\&=CF(\sec^2 2\psi)\lambda_{\min}/P\sin\psi.\end{aligned}\qquad(8.6)$$

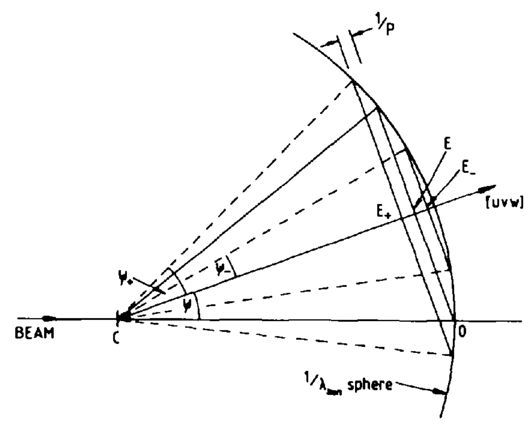

Fig. 16. Intersections of zone plane and its delimiting planes with $1/\lambda_{\min}$ sphere.

Hence we may estimate

$$\lambda_{\min}=[(GG_\pm/CF)P\sin\psi]/\sec^2 2\psi.\qquad(8.7)$$

As a check on the working, we note that the expressions (8.2) and (8.6) for $GG_\pm$ are equal when $\psi=\theta_c=\sin^{-1}(\lambda_{\min}D^*/2)$.

8.4. *General directions*

Let F be the centre of the detector and T any spot on a zone conic, Fig. 15(*a*). Let FT meet either of the envelopes surrounding the clear region at $T'_{\rm rad}$, so that the radial gap is $TT'_{\rm rad}$. Let $TT'_{\rm tgt}$ be the gap in the direction at right angles to FT. For a small gap, T and $T'_{\rm tgt}$ will have the same θ.

When $\theta>\theta_c$, it may be shown that the angular separations, if small, between the beams corresponding to T and $T'_{\rm rad}$ and between T and $T'_{\rm tgt}$ are

$$\gamma_{\rm rad}=2/PD^*\sin\eta\qquad(8.8)$$

and

$$\gamma_{\rm tgt}=2\sin\theta/PD^*\cos\eta,\qquad(8.9)$$

where η is the angle between the diffraction plane and the zone plane, given by $\sin\eta=\cos\psi/\cos\theta$. For the maximum diameter of an ellipse $\theta=\psi$ and $\sin\eta=1$. $\gamma_{\rm rad}$ (8.8) then reduces to the previously given (8.1).

If the conic has $\psi=\pi/2$, it is a straight line through the centre of the detector, Fig. 15(*b*). Only $\gamma_{\rm tgt}$ is meaningful and $\eta=0$. We obtain

$$\gamma_{\rm tgt}=2\sin\theta/PD^*\qquad(8.10)$$

and since $CT=CF\sec 2\theta$

$$TT'_{\rm tgt}=2CF\sin\theta\sec 2\theta/PD^*.\qquad(8.11)$$

When $\theta<\theta_c$, the analysis of § 8.3 and Fig. 16 may be applied to a conic with $\psi=\pi/2$ and $\cos\psi=0$. E then coincides with C and we obtain $\cos\psi_\pm=\lambda_{\min}/P$. The tangential gap at any point T, with Bragg angle θ, of the straight line conic is

$$TT'_{\rm tgt}=CF\sec 2\theta\cos\psi_\pm=\lambda_{\min}CF\sec 2\theta/P.\qquad(8.12)$$

The expressions (8.11) and (8.12) for $TT'_{\rm tgt}$ are equal when $\theta=\theta_c$. At small θ the gap $TT'_{\rm tgt}$ is by (8.12) practically independent of θ and is of magnitude $TT'_{\rm tgt}=\lambda_{\min}CF/P$.

8.5. *Comparison of internal and external separations*

In a Laue pattern, conics with a high density of spots are bordered by large clear regions. This observation is made more precise by the analysis of this paper.

When $\psi > \theta_c$, the minimum internal angular separation between adjacent beams in a conic is

$$\gamma_{\min} = 2P \sin \psi / D^{*2} V. \tag{7.2}$$

The minimum external angular separation across the clear border region at the major diameter of an ellipse is

$$\gamma_{\text{rad}} = 2/PD^*. \tag{8.1}$$

When $\theta > \theta_c$ and $\psi = \pi/2$, the minimum angular separation between adjacent beams in a straight-line conic is

$$\gamma_{\min} = 2P/D^{*2} V \tag{8.13}$$

and the minimum angular separation sideways across the clear region is

$$\gamma_{\text{tgt}} = 2 \sin \theta / PD^*. \tag{8.10}$$

When $\theta < \theta_c$, the corresponding separations are obtained by replacing D^* by $2 \sin \theta / \lambda_{\min}$ in the above equations.

We see that the internal separations depend on $P \sin \psi$, whereas the external border width depends on $1/P$. Hence, apart from the $\sin \psi$ factor, there is an inverse relation between the internal and external separations. This is another way of expressing the point made in § 6.2 that when three mutually adjacent conjugate rays are considered, only one of the inter-ray angles can be very small.

The ratio between the external γ_{rad} (8.1) and the internal $\gamma_{\min}$ (7.2) is $D^* V / P^2 \sin \psi$. For comparison with the argument in § 6.2, we may take $V = 1/V^* = 1/a^{*3}$ and $P = 1/a^*$, thus making the ratio $D^*/a^* \sin \psi$, which is much greater than 1. Apart from the factor $\sin \psi$, which arises from the distinction between diffracted beams and rays, this ratio is the same as appeared in § 6.2 for the ratio between α_{31} and the smallest inter-ray angle α_{23}.

A further point related to external separations and concerning visible rings surrounding prominent conics is discussed in Appendix 3.

9. Main findings and discussion

9.1. *Summary of chief theoretical results*

There are two main aspects to the angular distribution of rays and diffracted beams presented above: general and local. The general aspects refer to the diffraction pattern as a whole and local to reflections in a particular zone or in a small region of that zone.

It comes as no surprise that the spatial density of reflections is everywhere proportional to $1/CF^2$, where CF is the crystal-to-detector distance and to $1/V^*$ where V^* is the reciprocal-cell volume. However, there is substantial variation in spatial density with diffraction angle θ; a prominent maximum occurs at $\theta_c = \sin^{-1}(\lambda_{\min} D^*/2)$ as shown in Fig. 4. The value of this maximum may be diminished by increasing $\lambda_{\min}$ and hence also θ_c, as shown by (3.5). Conversely, (3.5) shows that a very small $\lambda_{\min}$ would lead to a greatly increased density at a very small θ_c.

More interesting results arise when considering local aspects. The most striking visual aspect of Laue patterns, namely the prominent conics on which the reflections lie, demarcated by clear spaces, is explained by an application of the Bravais theory of lattices, §§ 6.2 and 8.5, which reveals that, for three mutually conjugate rays (and their corresponding diffracted beams), only one inter-ray angle can be very small; the other two angles must be substantially larger. This immediately accounts for the visually apparent one-dimensional clustering of reflections along the arcs of conics and the way in which the most prominent densest arcs are flanked by clear spaces. That is, the local spatial distribution is inherently one dimensional in character, rather than two dimensional. Indeed, for longer CF distances the great majority of reflections that lie closer than some specified small value - the spatial overlaps - lie on a relatively small number of conics, as illustrated in Figs. 8(*a*) and (*b*).

Second, for $\theta > \theta_c$, the average angular separation of beams along a conic arc is constant for a given zone and a given crystal orientation, (7.3). The conics with the lowest angular separation (highest linear density) are readily picked out by eye [*e.g.* Figs 1(*a*) and 14] and are found to have the lowest values of $P \sin \psi$, as (7.3) predicts. As the crystal is reoriented with respect to the X-ray beam, only the values of $\sin \psi$ change.

Third, the derivation of the inter-ray angle $\alpha_{12} = A^*/d_1^* d_2^*$, (6.2), shows that when d_1^* is particularly small, as it must be for multiples, then α_{12} is particularly large. That is, multiples (nodals) have a larger angular separation from their nearest neighbours; they are surrounded by a clear space that makes them visually apparent. An important result is that multiples cannot be adjacent; they must be separated by at least one single (§ 6.4).

Fourth, the lowest possible inter-ray angle between a pair of singles is A^*/D^{*2}, but is n times larger between a single and an n-tuple (§ 6.4). That is, the vast majority of all inter-ray angles below a particular value are associated with pairs of adjacent single rays. Thus as noted previously (Helliwell, 1985), the reflections involved in energy overlaps - the multiples - form a set largely distinct, except at short CF distances, from those involved in spatial overlaps, which are mostly singles. However, for CF distances such that similar numbers of reflections are involved in each category, both kinds of overlap mostly involve the same prominent zones. [For a demonstration, compare Figs. 5(*c*) and (*d*) of Helliwell (1985).] In essence, spatial overlaps occur only in dense zone conics, each of which has an appreciable number of reflections, and by CHM1 for $\theta < \theta_2$ a significant fraction of reflections in these zones are necessarily multiples.

Fifth, the gaps bordering conics may be used to estimate D^* and $\lambda_{\min}$ (§ 8). However, it has been found that a development of the method using gnomonic projections is even more effective (Cruickshank, Carr & Harding, 1991).

9.2. *Practical implications*

One clear experimental goal is to maximize the number of reflections for which precise intensities can be measured. Some variables that control the spatial density of reflections, such as V^* and D^*, are fixed by the specimen; others, like the orientation of the crystal, have only a relatively minor effect. The selection of a particular orientation may be necessary to minimize spatial overlaps in a particular zone (or for other reasons), but it has essentially no overall effect on the number of spatial overlaps (except in certain unusual cases where one cell dimension is very different from the other two). Some alleviation of spatial overlaps may be achieved by increasing $\lambda_{\min}$, but this is at the expense of reducing the total number of stimulated RLPs and by (1.2) this number is proportional to $(\lambda_{\max} - \lambda_{\min})$.

By far the major effects on spatial overlap come from the crystal-to-detector distance *CF* and the spot-to-spot resolution capability. Table 2 in § 3.4 showed that there was a balance, on moving the plate further back, between the gain from the separation of spatially overlapped spots and the loss of RLPs due to diffracted beams missing the plate. Obviously the optimum *CF* distance depends on the plate size, the spot-resolution capability and the cell dimensions. With the pea lectin parameters and a resolution capability of 0·35 mm, when the energy overlaps are also considered, less than half of all stimulated RLPs are measurable. With doubled cell dimensions (Table 4) but the same 59·3 mm plate radius, less than 30% of the RLPs can be recovered even with 0·2 mm resolution; many beams miss the more distant plate.

Since 0·2 mm is an ambitious resolution criterion, it is self evident that changes to the detector such as increase in size are potentially very important. Spatial resolution can in effect be greatly improved also by a superior profile-fitting algorithm that enables individual integrated intensities to be extracted from closely adjacent or partially overlapping reflections (Shrive, Clifton, Hajdu & Greenhough, 1990).

There is also scope for novel detector arrangements. One of us (JRH) has suggested the use of a multiple film holder with each film separated by 10 mm or more in a 'toast rack' arrangement. This idea was based on observations (later rationalized by § 3.3) that the shorter-wavelength spots are predominantly the ones involved in the spatial overlaps around θ_c and that the longer-wavelength spots are less involved in spatial overlaps and occur predominantly at large θ. In the 'toast rack', the short-wavelength spots, although overlapped on the front film, will penetrate to the rear films where they will often be separated. The longer-wavelength singles, provided they do not lie in unacceptably high-density regions on arcs of low $P \sin \psi$, will be recorded on the front film, which subtends a large value of θ. The benefits of this arrangement have been assessed so far by computer simulation. It seems that it is possible to increase greatly the number of measurable RLPs as compared with the standard multiple film pack (Helliwell & Higashi, 1991).

An alternative arrangement suggested by another of us (KM) is to use a cylindrical detector whose axis coincides with the incident X-ray beam. In this way reflections at low θ automatically intercept the detector at a large value of *CF*.

Two caveats should be mentioned. The present treatment is based on an accessible region of reciprocal space defined by D^*, $\lambda_{\max}$ and $\lambda_{\min}$. In reality these are 'soft' limits, so that there will be a fuzziness in any results dependent on these parameters. Our treatment concerns accessible points in the reciprocal lattice. Actual reflections involve intensity factors, with which we have not been concerned. Experimentally reflections may be unobserved because of low intensity and this makes the D^* boundary particularly fuzzy and possibly anisotropic.

Secondly, our theories deal with rays and diffracted beams as though they were geometrical lines; yet in practice the incident X-ray beam is not exactly parallel, the X-ray collimator is of finite diameter and the crystal may exhibit isotropic or non-isotropic mosaic spread. All these effects increase the area of the spot profile on the detector and hence diminish the ease with which adjacent reflections can be distinguished.

Mosaic spread is often appreciable for small crystals (Andrews, Hails, Harding & Cruickshank, 1987) and can suddenly increase during time-resolved macromolecular crystallographic studies. Bartunik & Borchert (1989) show how the optimum Laue wavelength bandwidth depends strongly on the crystal mosaicity. Polychromatic neutron diffraction will be more prone than X-ray diffraction to spatial overlap problems because of larger beam divergence. A knowledge of the ideal angular distribution of reflections is nevertheless a basic requirement in such cases. Happily in many synchrotron Laue studies of macromolecular crystals by ourselves and others, the spots on the films are remarkably small and the addition of the concept of a spot-to-spot resolution capability to the ideal geometrical point-and-line theory yields very satisfactory understanding.

DWJC is greatly obliged to the former University Grants Committee for their pressure on UMIST to induce him to take premature retirement from employment and thus to free him for a life without duties. He thanks UMIST, the SERC Daresbury Laboratory and the Universities of York, Cornell and Manchester for subsequent hospitality in research environments and the Universities Superannuation Scheme for a pension. JRH thanks the Science and Engineering Research Council (SERC) for grant support, the SERC Daresbury Laboratory for synchrotron-radiation facilities and the Universities of York and Manchester for support. The Royal Society and the Hasselblad Foundation have also provided generous grants. DWJC and JRH thank Dr M. M. Harding for discussions on the Laue method and Dr T. Higashi and Dr P. D. Carr for computer simulations. KM thanks NIH for their support of his research at Cornell through grant RR-01646. In conclusion, we wish to express our appreciation of the expositions of the Laue method given in the books of Wyckoff (1924) and Amorós, Buerger & Amorós (1975).

APPENDIX 1
Conic geometry

If ψ is the inclination of the zone axis to the incident beam and the detector is normal to the incident beam the conic on the detector has eccentricity $e = \sin\psi/\cos\psi = \tan\psi$ (Sommerville, 1937). More generally, for an inclined detector $e = \sin\nu/\cos\psi$, where ν is the angle between the cone axis and the detector normal.

When $\psi < \pi/4$, the conic on a normal detector is an ellipse. If R is the centre of the ellipse, the major axis RF [Fig. 9(*a*)] has length

$$a = \tfrac{1}{2}CF\tan 2\psi,$$

where CF is the crystal-to-detector distance. The minor axis has length

$$b = a(1-e^2)^{1/2} = \tfrac{1}{2}CF\tan 2\psi(1-\tan^2\psi)^{1/2}.$$

[The expressions for a and b given by Amorós *et al.* (1975), p. 102 are incorrect.] For small ψ, $b/a \simeq (1-\psi^2/2)$. Note that, if CF is fixed, a and b are not independent parameters. The equation of an arbitrary ellipse on a flat detector may be determined by two parameters, ψ and an azimuthal orientation parameter. Note also that the centre R of the ellipse is not the point of intersection S of the zone axis with the detector.

The foci f_1, f_2 of the ellipse are distant

$$\pm ae = \pm\tfrac{1}{2}CF\tan 2\psi\tan\psi$$

from the centre R. Geometrically, by the Dandelin construction (Sommerville, 1937), f_1 is the point of contact of a sphere inscribed in the cone in front of the detector and f_2 is the point of contact of a sphere escribed in the cone behind the detector.

When $\psi = \pi/4$, the conic is a parabola, whose focus is distant $\tfrac{1}{2}CF$ from the plate centre F.

When $\psi > \pi/4$, the conic is a hyperbola passing through F with eccentricity $e = \tan\psi > 1$ and whose parameters are

$$a = -\tfrac{1}{2}CF\tan 2\psi \quad\text{and}\quad b = a(e^2-1)^{1/2}.$$

The asymptotic half-angle $\alpha = \tan^{-1}(b/a) = \sec^{-1}(\tan\psi)$.

APPENDIX 2
Accessible areas of zones

For a given zone, the conic on a flat detector is an ellipse when the zone-axis inclination $\psi < 45°$ and a hyperbola when $\psi > 45°$. However, the shape of the accessible region of the zone plane depends on ψ in quite a complicated fashion. As earlier we define $\theta_c = \sin^{-1}(\lambda_{\min}D^*/2)$, $\theta_m = \sin^{-1}(\lambda_{\max}D^*/2)$ and $\theta_2 = \sin^{-1}(\lambda_{\max}D^*/4)$. The latter corresponds to the θ at which $d_e^*/d_i^* = 2$; for $\theta > \theta_2$ some rays with inner points inside the external surface S_e will have no points in the accessible region. The missing rays will widen the spacing between observable beams.

We distinguish three situations.

Case I $\psi < \theta_c$.
Case II $\theta_c < \psi < \theta_m$.
Case III $\psi > \theta_m$.

In case I, Figs. 17(*a*), (*b*), the accessible region of the zone plane is a circle of diameter $2\sin\psi/\lambda_{\min}$ passing through the origin minus a circle of diameter $2\sin\psi/\lambda_{\max}$ also passing through the origin. The accessible area is thus

$$\pi\sin^2\psi(1/\lambda_{\min}^2 - 1/\lambda_{\max}^2) \qquad (A.1)$$

and the number of accessible RLPs is approximately this area divided by $A^*(uvw) = P[uvw]/V$.

For small ψ, the ellipse in the Laue pattern is practically a circle. The number of spots varies as ψ^2/P and the linear spot density averaged over the whole circumference of the conic varies as ψ/P since the circumference is proportional to ψ. At any particular θ on the conic the spot density is proportional to $\theta^2/P\psi$. Thus in case I conditions, a zone conic is densest when $\psi = \theta_c$ and the local density is greatest for θ near θ_c. (The discussion of Fig. 14 in § 7.2 provides some illustration of these points.)

In case II, Figs. 17(*c*), (*d*), the circle of diameter $2\sin\psi/\lambda_{\min}$ is truncated for $\theta > \theta_c$ by the arc of the circle of radius D^* centred at the origin. θ_c corresponds to an azimuthal angle α_c in the zone plane given by $\sin\alpha_c = \sin\theta_c/\sin\psi$. The accessible area is

$$D^{*2}(\pi/2-\alpha_c)+(\sin^2\psi/\lambda^2_{\min})[(2\alpha_c-\sin 2\alpha_c)] -\pi\sin^2\psi/\lambda^2_{\max}. \qquad (A.2)$$

The linear spot density along the arc of the Laue conic is greatest when $\theta_c<\theta<\theta_2$. Increase of ψ lowers the density for a given zone.

In case III, Figs. 17(*e*), (*f*), the circle of diameter $2\sin\psi/\lambda_{\max}$ is also truncated by part of the D^* circle. The azimuthal angle α_m corresponding to θ_m is given by $\sin\alpha_m = \sin\theta_m/\sin\psi$. The accessible area is

$$D^{*2}(\alpha_m-\alpha_c)+\sin^2\psi[(2\alpha_c-\sin 2\alpha_c)/\lambda^2_{\min} -(2\alpha_m-\sin 2\alpha_m)/\lambda^2_{\max}]. \qquad (A.3)$$

When $\psi=\pi/2$, the conic is a straight line, $\alpha_c=\theta_c$, $\alpha_m=\theta_m$ and the area becomes

$$D^{*2}(\theta_m-\theta_c)+[(2\theta_c-\sin 2\theta_c)/\lambda^2_{\min} -(2\theta_m-\sin 2\theta_m)/\lambda^2_{\max}]. \qquad (A.4)$$

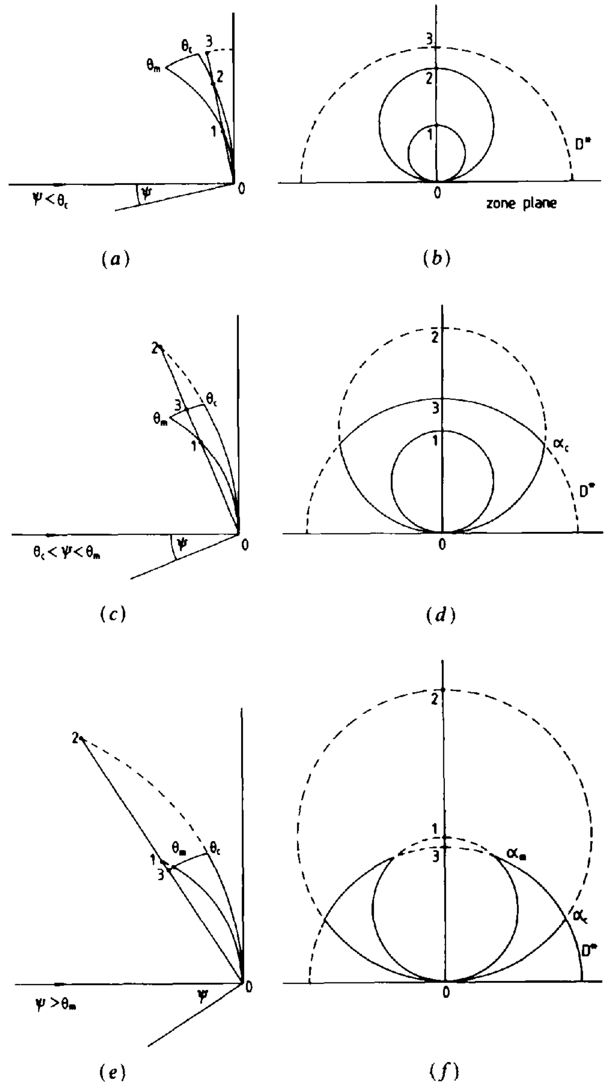

(*a*) (*b*)

(*c*) (*d*)

(*e*) (*f*)

Fig. 17. Accessible areas of zones. $O1=2\sin\psi/\lambda_{\max}$, $O2=2\sin\psi/\lambda_{\min}$, $O3=D^*$. (*a*), (*b*) Case I, $\psi<\theta_c$. (*c*), (*d*) Case II, $\theta_c<\psi<\theta_m$. (*e*), (*f*) Case III, $\psi>\theta_m$. (*a*), (*c*), (*e*) are sections of the accessible region of reciprocal space in the plane of the incident beam and zone axis. In (*b*), (*d*), (*f*) the continuous curves indicate the accessible areas of the zones.

In case III the linear spot density along the conic is greatest when $\theta_c<\theta<\theta_2$ and the average angular separation between spots then has value $3{\cdot}29(2P\sin\psi/D^{*2}V)$. Obviously the separations are largest when $\psi=\pi/2$.

Note that if ψ is varied by rotation of the zone plane about its line of intersection with the tangent plane to the Ewald spheres, a case I orientation will contain no RLPs in common with a case III orientation (since the accessible areas do not overlap).

APPENDIX 3

Visible rings surrounding prominent conics

In Fig. 1(*a*) the large clear gap outside the [011] conic corresponds to the absence of accessible RLPs between the **h** . **u** = 0 and **h** . **u** = 1 planes. Moving outwards from the nodal spot *b* along the reflections of the [100] and [$\bar{1}$11] zones, the eye detects a second ring. This corresponds to the intersection of the plane **h** . **u** = 2 with the external surface S_e. For the families of conics radiating from spot *b*, the spots lying between the **h** . **u** = 1 and **h** . **u** = 2 intersections are singles with d^* decreasing from D^* to $D^*/2$ (since $\theta>\theta_c$). On passing through the **h** . **u** = 2 intersection, these [$\bar{1}vv$] conics give rise to an alternation of doubles and singles, with d^* for the singles and for the outer points of the doubles again decreasing from D^*. Interleaved between the [$\bar{1}vv$] conics are a family of [$\bar{2}vv$] conics, which make their appearance at the second ring. Other families, [$\bar{3}vv$] and [$\bar{3}$,2*v*,2*v*], start from the third ring, which corresponds to the **h** . **u** = 3 intersection. It will also be realized, by Fig. 10, that for $\theta>\theta_c$ the number of reflections in each of the [$\bar{1}vv$] conics between the first and second rings is approximately equal to half the maximum order of the nodal *b* from which they radiate.

References

Amorós, J. L., Buerger, M. J. & Amorós, M. C. (1975). *The Laue Method.* New York: Academic Press.

Andrews, S. J., Hails, J. E., Harding, M. M. & Cruickshank, D. W. J. (1987). *Acta Cryst.* **A43**, 70-73.

Bartunik, H. D. & Borchert, T. (1989). *Acta Cryst.* **A45**, 718-726.

Bragg, W. L. (1975). *The Development of X-ray Analysis*, edited by D. C. Phillips & H. Lipson. London: Bell.

BRAVAIS, M. A. (1949). *On the Systems Formed by Points Regularly Distributed on a Plane or in Space.* Translated by A. J. SHALER from *Journal de l'Ecole Polytechnique, Cahier* 33, Vol. 19, pp. 1-128, Paris (1850). Washington, DC: American Crystallographic Association.
BROOKS, I., MOFFAT, K. & CRUICKSHANK, D. W. J. (1991). In preparation.
CLIFTON, I. J., CRUICKSHANK, D. W. J., DIAKUN, G., ELDER, M., HABASH, J., HELLIWELL, J. R., LIDDINGTON, R. C., MACHIN, P. A. & PAPIZ, M. Z. (1985). *J. Appl. Cryst.* **18**, 296-300.
CRUICKSHANK, D. W. J. (1991). In preparation.
CRUICKSHANK, D. W. J., CARR, P. D. & HARDING, M. M. (1991). In preparation.
CRUICKSHANK, D. W. J., HELLIWELL, J. R. & MOFFAT, K. (1987). *Acta Cryst.* A**43**, 656-674.
HELLIWELL, J. R. (1984). *Rep. Prog. Phys.* **47**, 1403-1497.
HELLIWELL, J. R. (1985). *J. Mol. Struct.* **130**, 63-91.
HELLIWELL, J. R., HABASH, J., CRUICKSHANK, D. W. J., HARDING, M. M., GREENHOUGH, T. J., CAMPBELL, J. W., CLIFTON, I. J., ELDER, M., MACHIN, P. A., PAPIZ, M. Z. & ZUREK, S. (1989). *J. Appl. Cryst.* **22**, 483-497.
HELLIWELL, J. R. & HIGASHI, T. (1991). In preparation.
HENRY, N. F. M., LIPSON, H. & WOOSTER, W. A. (1951). *The Interpretation of X-ray Diffraction Photographs.* London: Macmillan.
JEFFREY, J. W. (1958). *Z. Kristallogr.* **110**, 321-328.
SHRIVE, A. K., CLIFTON, I. J., HAJDU, J. & GREENHOUGH, T. J. (1990). *J. Appl. Cryst.* **23**, 169-174.
SOMMERVILLE, D. M. Y. (1937). *Analytical Conics.* London: Bell.
WYCKOFF, R. W. G. (1924). *The Structure of Crystals.* New York: Chemical Catalog Co.

Acta Cryst. (1991). A**47**, 373-381

Automatic Solution and Refinement of Crystal Structures by Means of the Package *UNIQUE*

BY G. CASCARANO AND C. GIACOVAZZO

Istituto per lo Sviluppo delle Metodologie Cristallografiche, CNR, c/o Dipartimento Geomineralogico, Campus Universitario, 70124 *Bari, Italy*

M. CAMALLI AND R. SPAGNA

*Istituto di Strutturistica Chimica 'G. Giacomello', Area della Ricerca del CNR, CP*10, 00016 *Monterotondo Stazione, Roma, Italy*

AND D. J. WATKIN

Chemical Crystallography Laboratory, 9 *Parks Road, Oxford OX*1 3*PD, England*

(*Received* 25 *June* 1990; *accepted* 16 *January* 1991)

Abstract

An automatic procedure for crystal structure solution and refinement has been devised. It is able to take decisions at each critical point of the analysis by taking careful account of all information available at that point. The procedure has been implemented into the package *UNIQUE* (*CRYSTALS*+*SIR*88) and has been applied successfully to a wide variety of crystal structures. In most cases, the complete structure is recovered and refined without any user intervention. *R* values usually lie in the range 0·08-0·15.

1. Introduction

Direct methods are today the most powerful method for solving crystal structures up to medium complexity. Programs usually stop with one or more sets of atomic coordinates selected by suitable figures of merit (FOM's). The chemical significance of each trial solution is then checked *via* atomic connectivity tables. Such analyses may be inconclusive when: (i) no prior information about the molecule is available; (ii) the map is uninterpretable because some atoms have been missed, false peaks are present or the molecular geometry is distorted in some way; (iii) an expected molecular fragment is recognized in the electron-density map but is shifted with respect to its correct position.

In each case structure-factor (SFC) and least-squares (LSQ) calculations together with Fourier (FOUR) methods provide an essential assessment of a trial solution and a powerful tool for the recovery of the complete structure from a partial one. Preparing data for SFC, LSQ and FOUR calculations is straightforward but tiresome and accompanied by the risk of user errors. Decisions have to be taken about: (*a*) reliability of the trial solution; (*b*) recognition of special atomic positions; (*c*) special procedures for hemimorphic space groups; (*d*) selection of a subset